Part I

1
III–Nitride Light-Emitting Diodes on Novel Substrates

Xian-An Cao

1.1
Introduction

During the past decade, III–nitrides, which form continuous and direct bandgap semiconductor alloys, have undergone a phenomenal development effort, and have emerged as the leading materials for light-emitting diodes (LEDs) with peak emission spanning from green through blue to ultraviolet (UV) wavelengths [1, 2]. High-brightness (HB) green and blue LEDs along with AlInGaP red and yellow LEDs complete the primary color spectrum and enable fabrication of large-scale full-color displays. Near-UV and blue LEDs, when used in conjunction with multiband or yellow phosphors, can produce white light and are therefore very attractive for solid-state lighting applications [3]. There are also plentiful ongoing endeavors to push emission wavelengths into the deep-UV regime for numerous applications including bioaerosol sensing, air and water purification, and high-density data storage.

One of the most defining features of the nitride material system is the lack of high-quality bulk GaN or AlN substrates. To date, all commercially available III–nitride LEDs are grown heteroepitaxially on foreign substrates such as sapphire and SiC. Si has also received some attention as the substrate for low-power LEDs due to its clear advantages of low cost and high quality. Many efforts have been devoted to developing high-quality buffer layers to accommodate the mismatch in lattice constant and thermal expansion coefficient between the epilayers and substrates. The presence of a high density of threading dislocations and large residual strain in the heteroepitaxial structures, along with strong piezoelectricity and large compositional fluctuation of the nitride alloys, give rise to some unique electrical and optical characteristics of current III–nitride LEDs [4].

Bulk GaN and AlN would be a nearly perfect match to LED heterostructures, and meet most substrate requirements. Homoepitaxial growth significantly reduces defect density and strain, and offers better doping and impurity control. These incentives are the driving force behind recent progress toward producing bulk GaN and AlN crystals [5, 6]. Some free-standing GaN substrates are now

Wide Bandgap Light Emitting Materials and Devices. Edited by G. F. Neumark, I. L. Kuskovsky, and H. Jiang

ISBN: 978-3-527-40331-8

commercially available, and preliminary results of homoepitaxy are encouraging. However, before large-area low-cost GaN wafers become available, sapphire and other foreign substrates will remain the common substrates for nitride LEDs due to the well-established heteroepitaxy technology.

In this chapter, key growth issues, design considerations, and the operation of III–nitride green, blue and UV LEDs on sapphire are described. An overview is then given that describes the growth and performance of nitride LEDs on other novel substrates, including Si, SiC, and bulk GaN and AlN. The influence of the substrates on the microstructual properties, electrical characteristics, light emission, and light extraction of the LEDs is discussed.

1.2 LEDs on Sapphire Substrates

1.2.1 LED Heteroepitaxy

Most commercially available III–nitride LEDs are grown on the *c*-plane of sapphire substrates. Large-area and high-quality sapphire is widely available in large quantities, and is fairly inexpensive. To date, much more knowledge and experience have been accumulated in the technology of growing III–nitrides on sapphire than on other substrates. Another advantage of using sapphire is its transparency to UV and visible light, reducing the parasitic light loss in the substrate. However, there are a few disadvantages associated with sapphire substrates. First, a large mismatch in lattice constant (~15%) and thermal expansion coefficient between nitride materials and sapphire gives rise to a high density of threading dislocations and biaxial stress in epitaxial layers. Second, sapphire is electrically insulating, making it necessary to fabricate LEDs in a lateral configuration. In this case, current spreading is a key device design consideration (described in Section 1.2.2). Third, sapphire has a relatively poor thermal conductivity, limiting heat dissipation in top-emitting LEDs. This, however, is less of a problem in flipchip LEDs, where heat is removed through the p-type contact.

Metal–organic chemical vapor deposition (MOCVD) has evolved as the dominant technique for growing III–nitride LEDs, not only on sapphire but also on other substrates [7]. However, the design of MOCVD reactors for nitrides is much less mature than for conventional III–V semiconductors. Currently both commercial and home-built reactors are used, and the growth process conditions vary widely. MOCVD is a nonequilibrium chemical process, in which gaseous precursors are injected from a precise gas-mixing manifold into a cold-wall reactor, where they react on a heated substrate. LED epitaxy is usually conducted under a low pressure. The common precursors include trimethylaluminum (TMAl), trimethylgallium (TMGa), and trimethylindium (TMIn) as the metal sources, and ammonia as the N source. Silane and bis-cyclopentadienyl-magnesium (Cp_2Mg) are used for n- and p-type doping, respectively. Hydrogen or nitrogen is used as the carrier gas.

The ideal growth temperatures for different layers of the LED structure are different: GaN is grown at 1000–1100 °C, AlGaN requires a slightly higher temperature, and InGaN is grown at a much lower temperature ~700–800 °C.

The realization of HB III–nitride LEDs on sapphire is based upon two epitaxy technology breakthroughs. The first was the demonstration of p-type conductivity in GaN. As-grown Mg-doped GaN has a very high resistivity due to the formation of Mg–H complexes. It was found that Mg can be activated by dissociating H from Mg using low-energy electron-beam irradiation [8] or annealing at >750 °C [9]. The second breakthrough was growing high-quality nitrides on sapphire using a thin low-temperature buffer layer [10]. The crystalline quality of GaN films grown directly on sapphire is generally poor due to the large mismatch between GaN and sapphire. Early work by several groups showed that GaN layers grown atop a thin AlN or GaN buffer layer greatly improved surface morphologies and crystalline quality [10, 11]. A buffer layer with a thickness of <100 nm, usually grown at ~500 °C, is critical to defect reduction and subsequent two-dimensional (2D) growth of device structures. Prior to the growth of the buffer, the sapphire substrate is usually nitridated by exposure to ammonia gas in the reactor [12, 13]. The nitridation process promotes GaN and AlN nucleation on sapphire and further improves the quality of the overlayer.

The first blue LED, reported by Nichia, consisted of InGaN/AlGaN double heterostructures (DHs) [14]. The active region was an InGaN layer codoped with Si and Zn, and an impurity-related transition was responsible for the blue emission. Their second-generation blue LEDs had an undoped InGaN single-quantum-well (SQW) active region, which exhibited efficient direct bandgap emission [15]. Figure 1.1(a) shows a typical layer structure of state-of-the-art green and blue LEDs, which consists of an InGaN/GaN multiple-quantum-well (MQW) active region [16, 17], an n-GaN lower cladding layer, a p-AlGaN upper cladding layer, and a p^+-GaN top contact layer. The p-AlGaN cladding layer is necessary to prevent electrons from escaping from the active region. The top surface is usually doped heavily with Mg to reduce the p-contact resistance. Similarly, deep-UV LEDs would have an AlGaN MQW active region sandwiched between n- and p-type AlGaN cladding layers with

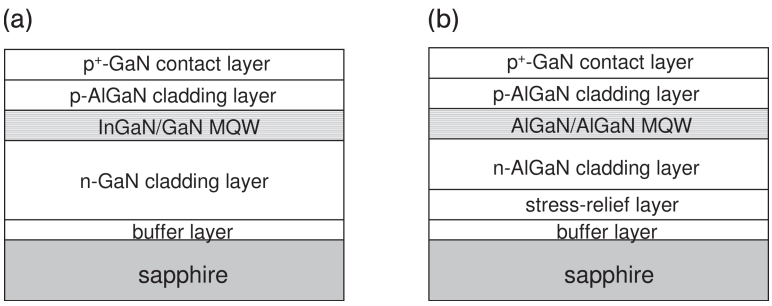

Fig. 1.1 Schematic of typical layer structures of state-of-the-art (a) InGaN-based visible LEDs and (b) AlGaN-based UV LEDs on sapphire substrates.

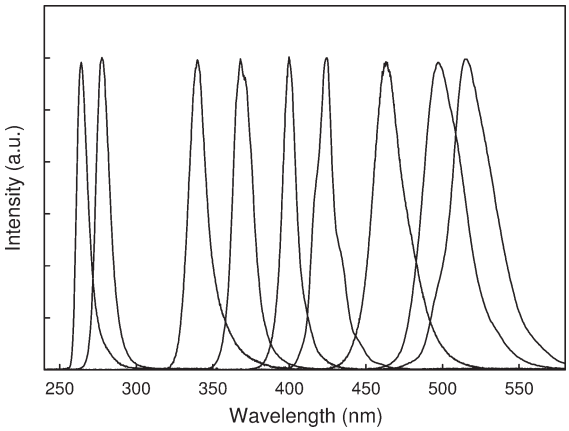

Fig. 1.2 Electroluminescence spectra of III–nitride MQW LEDs grown on sapphire substrates using MOCVD.

a higher Al content (Fig. 1.1(b)) [18, 19]. Figure 1.2 illustrates a series of electroluminescence (EL) spectra of III–nitride MQW LEDs made on sapphire with the MOCVD technique and with peak emission ranging from green to deep-UV. The green and blue LEDs have a much larger full width at half-maximum (FWHM) of ~30 nm than the UV LEDs. The spectral broadening is believed to arise from large compositional inhomogeneity in the InGaN active regions [4].

During the LED overgrowth, the epilayer is essentially relaxed rather than being strained to lattice-match to the sapphire. However, a large biaxial compressive stress may be generated upon cooling to room temperature due to the larger thermal expansion coefficient of sapphire [20]. The actual magnitude and sign of the stress are a function of the growth conditions, and depend largely on the thickness and doping level of the thick n-type cladding layer. It has been found that excessive Si doping may change the stress from compressive to tensile [21], which promotes wafer bowing and film cracking, and limits the maximum size of wafers and the thickness of LED structures. Compared to GaN epilayers, AlGaN films grown on sapphire are more subject to a large residual stress. To improve strain management, state-of-the-art deep-UV LEDs are grown on a thick AlN template with an additional AlN/AlGaN superlattice stress-relief layer [18, 19]. Zhang et al. [22] reported a pulsed atomic-layer epitaxy technique, which considerably suppresses gas-phase reaction, enhances adatom surface migration, and produces AlN and AlGaN template layers with reduced alloy disorder and improved surface morphology. The high-quality stress-relief layer has proven to be crucial for the subsequent growth of High-Al content AlGaN LED structures.

Despite the use of a buffer layer to accommodate the large lattice mismatch between nitrides and sapphire, a very high level of threading dislocations (10^8–$10^{10}\,cm^{-2}$) is present within LED heterostructures [23]. Some traverse vertically from the epilayer/substrate interface to the top layer and, depending on the growth conditions of the capping layer, may terminate by forming various types of surface

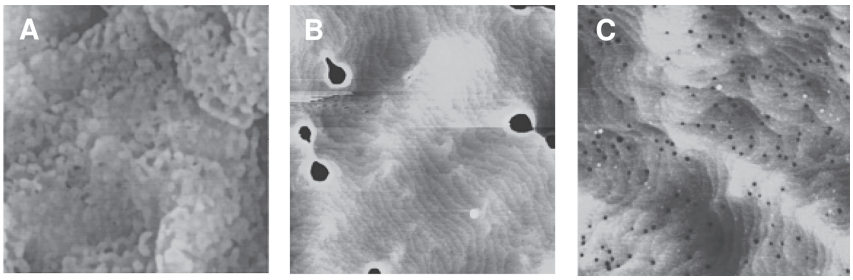

Fig. 1.3 AFM images (2 μm × 2 μm) of three representative InGaN/GaN MQW LEDs grown on sapphire using MOCVD.

defects. Figure 1.3 shows atomic force microscopy (AFM) images of three InGaN/GaN MQW LEDs on sapphire with different surface morphologies. The root-mean-square (rms) surface roughness of these samples is in the range of 0.4–0.8 nm over a $2 \times 2\,\mu m^2$ area. The surface of LED A is microscopically rough but free of obvious pits, whereas LEDs B and C present a large number of surface defects. On sample B, there are ~$1.5 \times 10^8\,cm^{-2}$ pits with hexahedral cone morphology and a size ~100 nm. LED C shows a swirled step structure and $4 \times 10^9\,cm^{-2}$ small surface pits, which are caused by the intersection of the top surface with the dislocations [24]. Cross-sectional transmission electron microscopy (TEM) showed that the densities of dislocations reaching the MQW active region in LEDs A, B and C were $6 \times 10^8\,cm^{-2}$, $3 \times 10^9\,cm^{-2}$, and $5 \times 10^9\,cm^{-2}$, respectively. In LED A, dislocation bending was found at 200–350 nm after the buffer layer, and a relatively small number of dislocations, mainly of edge character, propagated to the top layer. The hexagonal pits in LED B, usually called V-defects, were found to form in either the p-GaN capping layer or the MQW region, and were connected to threading dislocations. Large strain at the GaN/InGaN interfaces and In-rich regions [25, 26], or impurity complexes, are believed to be the cause of their formation [27].

The dislocation densities in III–nitride LEDs grown on sapphire are far higher than those observed in working LEDs based on conventional III–V semiconductors. GaAs-based LEDs with a dislocation density $>10^4\,cm^2$ would not show any band-edge emission [28]. The fact that efficient blue and green LEDs can be made with highly defective InGaN materials suggests that threading dislocations do not act as efficient nonradiative recombination centers [29, 30]. This is supported by the finding that blue and green LEDs grown on a high-quaity, laterally overgrown GaN template with a dislocation density of ~$7 \times 10^6\,cm^{-2}$ had an external quantum efficiency similar to LEDs grown on a regular buffer layer [31]. It is now well accepted that In-rich quantum-dot-like (QD-like) regions self-formed in InGaN alloys due to strong compositional fluctuation, enhance carrier localization and radiative processes [4]. The localization effects, which are however lacking in high-quality AlGaN alloys, result in some unique EL behaviors of InGaN LEDs, and will be detailed in Sections 1.2.4 and 1.2.5.

1.2.2 Current Spreading

Due to the insulating substrate, InGaN/GaN LEDs grown on sapphire must be fabricated in a lateral configuration. A mesa is defined using plasma etching so that the n-type electrode can be deposited on the exposed n-GaN cladding layer, whereas the p-type contact is formed atop the p-GaN layer. The resistivity of the top p-GaN layer is typically several orders of magnitude higher than that of the n-type cladding layer. It is therefore necessary to add an additional conducting layer to spread current to regions not covered by the p-type bonding pad. In top-emitting LEDs, current spreading on the p-side usually relies on the use of a semitransparent contact covering the entire p-GaN [32, 33]. The current spreading layer also functions as an ohmic contact and light extraction window, and therefore must be transparent to the emitted light.

To reduce current nonuniformity, lateral current paths as determined by the spacing between the p-type and n-type electrodes should be smaller than the current spreading length, which is the length where current density drops to 1/e of that under the p-pad or at the mesa edge. The current spreading length L_s in a top-emitting LED is given by

$$L_s = (r_c + \rho_p t_p)^{1/2} \left| \frac{\rho_n}{t_n} - \frac{\rho_t}{t_t} \right|^{-1/2} \tag{1.1}$$

where ρ_p, ρ_n, ρ_t, t_p, t_n, and t_t are the respective resistivity and thickness of the p-GaN, n-GaN, and semitransparent contact, and r_c is the specific contact resistance of the p-contact [33]. It is clear that a uniform current distribution can be achieved when the n-type and p-type current spreaders have an identical sheet resistance (i.e., $\rho_t/t_t = \rho_n/t_n$) [32]. Current tends to crowd toward the p-pad or mesa edge adjoining the n-type electrode when this condition is not met. Current crowding may lead to a nonuniform light emission and self-heating, thus reducing the quantum efficiency and accelerating LED degradation. With increasing mesa size, current crowding becomes more severe. Novel mesa geometries, such as interdigitated mesas or multiple isolated mesas with a width less than L_s, must be used to alleviate this problem [34]. These types of designs also enjoy the advantage of good scalability, which is critical for developing large-area high-power LEDs.

A number of semitransparent contacts comprising a thin metal film have been investigated [35–39], among which a bilayer Ni/Au thin film is the most extensively used. It was found that the contact resistance of an Ni/Au contact to p-GaN can be substantially reduced by annealing the contact in an oxygen ambient to form NiO/Au [35]. The resultant NiO embedded with Au islands is believed to be a low-barrier contact to p-GaN [36], with a specific contact resistance in the 10^{-3}–$10^{-4}\,\Omega\,cm^2$ range. The oxidized Ni/Au is electrically conducive and semitransparent at visible wavelengths. Both the conductivity and transparency are strong functions of the Ni/Au content ratio. Figure 1.4 shows the sheet resistance and light transmission of Ni (5 nm)/Au films with varying Au thickness before and

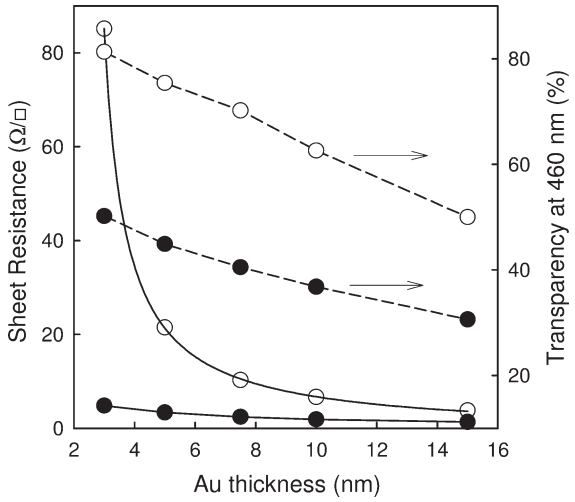

Fig. 1.4 Sheet resistance (solid lines) and light transmission (dashed lines) of Ni(5 nm)/Au films with varying Au thickness before (solid dots) and after (open dots) 550 °C annealing in air.

after a 550 °C anneal in air. The transparency is improved by ~60% after the anneal, and decreases rapidly with increasing Au thickness, whereas the resistance increases dramatically with decreasing Au content. Providing that the sheet resistance of the n-GaN layer in typical blue LEDs is ~20 Ω/□, the optimal Au thickness is 5–6 nm from the current spreading viewpoint. At this thickness, the Ni/Au film is >70% transparent at 460 nm, and forms a low-resistance ohmic contact to p-GaN.

In flipchip LEDs, the current on the p-side spreads in a thick ohmic metal, which also functions as a reflective mirror. Assuming negligible resistance of the p-metal, the current spreading length can be expressed as [40]:

$$L_s = \left((r_c + \rho_p t_p) \frac{t_n}{\rho_n} \right)^{1/2} \tag{1.2}$$

In this case, current tends to crowd at the edge of the mesa contact, and current density decreases exponentially with increasing distance from the mesa edge. Equation (1.2) shows that L_s can be increased by reducing the resistivity or increasing the thickness of the n-type cladding layer. In AlGaN-based deep-UV LEDs, L_s may be one order of magnitude smaller than in typical blue LEDs due to the low conductivity of high-Al AlGaN materials. Flipchip UV LEDs grown on sapphire are therefore more subject to current crowding and localized heating problems [41]. Interdigitated mesa structures or small mesa arrays must be employed to mitigate these problems.

1.2.3 Carrier Transport

Transporting electrons and holes from the current spreading layers to the QW active region is an essential step to generate light in the active region. Interfacial potential barriers and defect states in the cladding layers are expected to have a pronounced influence on the carrier transport dynamics. In a semiconductor p–n junction, the forward I–V characteristics at moderate bias can be described by the conventional Shockley model:

$$I = I_0 \exp(qV/nkT) \tag{1.3}$$

where I_0 is the saturation current, q is the electron charge, k is Boltzmann's constant, and T is the absolute temperature [42]. The ideality factor n, which is correlated with the slope of the semilogarithmic I–V plot, has a value between 1 and 2, indicating the coexistence of diffusion current ($n = 1$) and recombination current through bandgap states in the space-charge region ($n = 2$). In LEDs with an MQW active region, the ideality factor value associated with the diffusion process may be different. Carriers must diffuse over about one-half of the total barrier to be injected into the QWs where they recombine radiatively or nonradiatively. Taking this into consideration, an ideality factor close to 2 can be expected in high-quality InGaN/GaN QW LEDs [43].

In addition to thermal diffusion and recombination, tunneling may be another important mechanism of carrier transport in typical nitride LEDs. This is the case for two reasons. First, a high density of bandgap states is present in the space-charge region providing the tunneling paths. Second, the n- and p-type cladding layers are usually heavily doped, and the quantum barrier layers may also be doped with Si to screen the large piezoelectric field. The depletion layer at the junction is therefore relatively thin, enhancing carrier tunneling through the potential barriers at heterointerfaces. Following the analysis of Dumin et al. [44], the nonradiative tunneling current in a p–n junction involving single level traps depends exponentially on the applied voltage:

$$I = CN_t \exp(qV/E) \tag{1.4}$$

where C is a constant containing the built-in potential, N_t is the trap density, and the energy parameter E in a p^+–n junction is given by:

$$E = \frac{2hq\sqrt{N_D}}{\pi^2\sqrt{m^*\varepsilon_s}} \tag{1.5}$$

where m^* is the effective carrier mass, ε_s is the semiconductor dielectric constant, N_D is the donor concentration, and h is Planck's constant. One simple model that can be considered is that of electron tunneling to traps in the p-type cladding layer, sometimes evidenced by the associated defect radiative emission, or hole tunnel-

ing to bandgap states in the MQW region, followed by radiative or nonradiative recombination. The excess current could also result from a more complex process involving multiple-level states. This is especially possible in III–nitride LEDs because the defect density is sufficiently high. Possible sources of electrically active states include dislocations, impurities, Ga or N vacancies, and antisites. As seen in Eq. (1.4), the tunneling current has little temperature sensitivity. The slope of the semilogarithmic *I–V* plot is expected to be temperature-independent, which is in contrast to temperature-dependent diffusion and recombination currents.

Figure 1.5(a) compares the forward *I–V* characteristics of the LEDs whose microstructural properties were described in Section 1.2.1. At high injection currents ($>10^{-3}$ A), the details of carrier transport cannot be identified due to a high series resistance. At low and moderate bias, the *I–V* behaviors of LEDs B and C can be represented by Eq. (1.4), suggesting the dominance of tunneling current. Both LEDs show two main exponential segments with different slopes, which may result from tunneling processes involving different deep-level states. The energy parameter E has a room-temperature value of ~220 meV at voltages of 0–1.7 V and 72–105 meV at voltages of 1.8–2.6 V. At moderate bias, the unrealistic ideality factors are 2.8 and 4 for LEDs B and C, respectively.

The low-bias forward *I–V* characteristic of LED A is also dominated by tunneling current. However, at moderate bias above 2.1 V, it can be modeled by the conventional drift-diffusion model as $I = I_0 \exp(eV/1.6kT)$. The dominance of diffusion–recombination current reflects the high quality of LED A, in agreement with earlier structural analysis. Defect-assisted tunneling current is significantly suppressed. This current component has a slope proportional to $1/1.6kT$, as seen in Fig. 1.5(b). Also shown in this figure are the changes of the characteristic energy at moderate bias in LEDs B and C with increasing temperature. While the E value in LED C is mostly temperature-independent, it decreases slightly with increasing tempera-

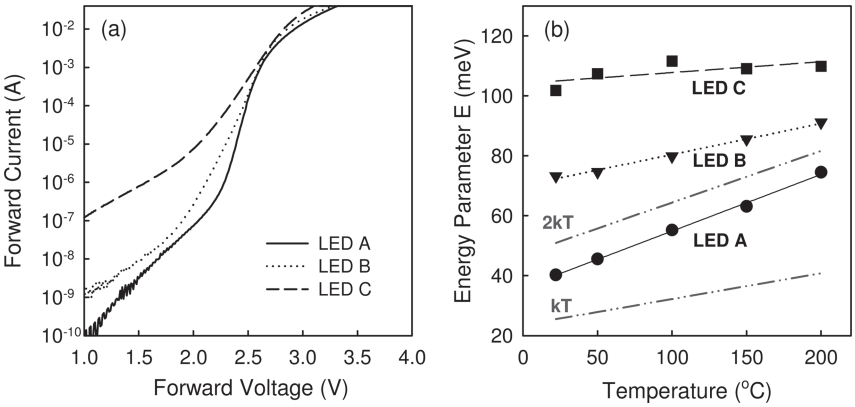

Fig. 1.5 (a) Forward *I–V* characteristics of three InGaN/GaN LEDs measured at room temperature. (b) The characteristic energy E at moderate bias as a function of measurement temperature.

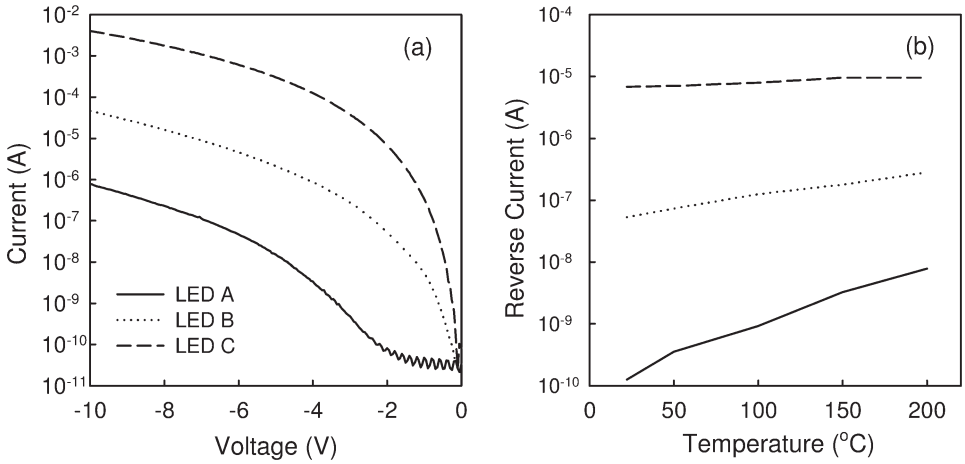

Fig. 1.6 (a) Reverse *I–V* characteristics of three InGaN/GaN LEDs measured at room temperature. (b) Reverse current at −2 V as a function of measurement temperature.

ture in LED B, indicating an increased contribution from diffusion–recombination current. The carrier injection is therefore a combination of tunneling, diffusion, and recombination processes. These results confirm a strong correlation between microstructural quality and the mechanism of current transport in III–nitride LEDs.

Reverse dark current in III–nitride LEDs usually scales with the junction area due to the dominant bulk leakage [45], and is many orders of magnitude higher than classical diffusion and generation–recombination currents in wide bandgap semiconductors. Figure 1.6(a) shows the reverse *I–V* characteristics for the three LEDs measured at 25 °C. The currents in LEDs B and C are strongly voltage-dependent but temperature-insensitive, as seen in Fig. 1.6(b). These are characteristic features of defect-assisted tunneling. Similar behaviors have also been found in conventional III–V diodes [46, 47], GaN p–n diodes [48], and double heterostructure (DH) blue LEDs [49]. At high reverse voltage, the data are in good agreement with band-to-band tunneling as predicated by the Zener tunneling model [46]. The electrons may tunnel from the p-GaN valence band to the n-GaN conduction band through to a thin depletion layer. The leakage current in LED A is several orders of magnitude lower. Carrier tunneling is not dominant until reverse bias >2 V, where there is a sudden increase in the slope. At bias <2 V, the leakage current is roughly an exponential function of temperature, indicative of the presence of thermal currents such as space-charge generation current.

1.2.4
Carrier Confinement and Localization

The confinement of injected carriers inside the MQW region increases the overlap of electrons and holes, resulting in much faster and more efficient radiative recom-

bination. To reduce the nonradiative recombination rate, the thickness of InGaN QWs should be less than the minority carrier diffusion length and is typically a few nanometers. The thin QWs also give rise to a high carrier density, which is preferred to suppress the nonradiative process by saturating defect states in the active region. The active layer is also designed to be thin to improve light extraction by reducing the internal band-to-band absorption.

In contrast to light-emitting devices based on conventional III–V semiconductors, InGaN-based LEDs are surprisingly efficient despite the existence of a high density of microstructural defects [29]. It is generally accepted that carrier localization effects that arise from spatially inhomogeneous indium distribution and QW thickness fluctuation play an important role in spontaneous emission from InGaN QW structures [4, 30, 50–55]. The InGaN compositional disorder occurs due to large differences in thermal stability and lattice parameters between GaN and InN. The localization effects improve the radiative recombination in two ways. First, QD-like In-rich regions in InGaN alloys trap carriers, forming localized excitons. This further enhances the overlap of electrons and holes, and their recombination rates. Second, localization effects prevent carriers from reaching defects, and thus reduce nonradiative recombination. Nanoscale QD-like structures in InGaN alloys have been measured directly by high-resolution TEM [53]. Submicron emission fluctuation resulting from In segregation was clearly observed from cathodoluminescence (CL) images [54]. The mean size of the QDs increases with increasing In content [55], indicating larger In compositional fluctuation and stronger localization effects in higher In content InGaN materials.

One characteristic feature of InGaN-based LEDs is a pronounced blueshift of the EL peak with increasing drive current. This can be attributed to the band filling of localized states at potential minima in the QW plane [4]. Figure 1.7 shows the EL spectra of an InGaN MQW green LED and an AlGaN MQW UV LED at 300 K as functions of injection current. The spectra of the green LED are much broader due to strong alloy broadening, and show a large blueshift of 54 meV as the current is increased from 0.1 mA to 20 mA. In contrast, the emission peak of the UV LED has a small FWHM of ~10 nm and is almost independent of injection current. These features suggest much smaller compositional fluctuation and weaker localization effects in the AlGaN MQWs. Carriers are, therefore, more likely to be trapped and recombine nonradiatively at defect states. This may partly explain why state-of-the-art deep-UV LEDs are much less efficient and less reliable than commercial InGaN LEDs. It has been found that the optical properties of AlGaN materials can be markedly improved by introducing a small amount of In to form quaternary AlInGaN alloys with enhanced localization effects [56–59]. In addition, by varying the compositions of quaternary alloys, the bandgap and lattice constant can be adjusted independently to achieve lattice-matched structures with a reduced dislocation density and piezoelectric field [60]. Efficient UV LEDs with peak wavelength 305–350 nm have been demonstrated based on AlInGaN MQW structures [57–59].

Another factor that may account for the EL blueshift is a large static electric field (up to a few MV cm^{-1}) in the InGaN QWs due to spontaneous and piezoelectric

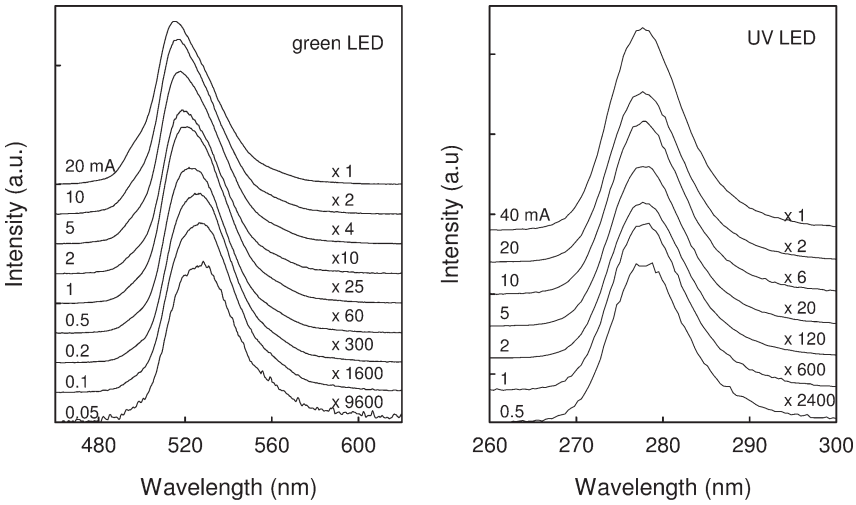

Fig. 1.7 EL spectra of an InGaN-based green LED and an AlGaN-based UV LED at 300 K as a function of injection current. The spectra are shifted in the vertical direction for clarity.

polarization [61, 62]. The latter arises from biaxial strain remaining in the heterostructures due to the lattice mismatch between the well and barrier layers. The electric field tilts the energy bands and separates electron–hole pairs into triangular potential wells formed at opposite sides of the QWs. When carriers are injected into the QWs and screen the polarization charges, the overlap of the electron–hole wavefunction is recovered, resulting in a blueshift of emission peak [63, 64]. In LEDs with thin InGaN QW active layers (≤3 nm), efficient carrier confinement and localization partially overcome the disadvantage of the piezoelectric effect. It has been found that doping the GaN quantum barrier layers with Si can effectively screen polarization-induced charges at the heterointerfaces [62, 65]. This technique is now extensively employed in commercial blue and green LEDs [66]. The EL blueshift in the green LED, as seen in Fig. 1.7, is therefore due largely to the band filling of localized states.

A better understanding of the role of localized states in the radiative process in InGaN-based LEDs can be gained by means of temperature-dependent luminescence measurement. Three LEDs (green, blue and UV) with a similar epitaxial structure, but varying In and Al contents in the MQWs and cladding layers, were characterized in the temperature range of 5–300 K. The respective nominal In mole fractions in the active regions were 0.35, 0.20 and 0.04. Figure 1.8 shows temperature-induced shifts of the peak energy of the LEDs operating at 1 mA. With decreasing temperature, a blueshift and then a redshift is seen for all LEDs, although the amounts of the shifts are different. The redshift in the UV LED between 77 and 200 K is as large as 50 meV. Considering that the temperature-

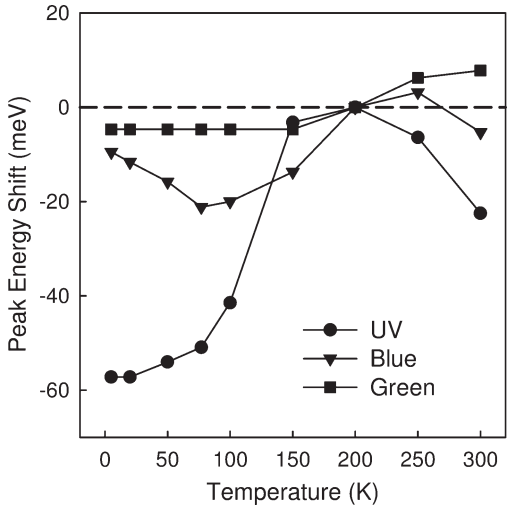

Fig. 1.8 Peak energy shift in InGaN/GaN MQW LEDs as a function of measurement temperature.

induced change of the GaN bandgap energy is ~26 meV, the actual displacement of the peak energy relative to the band edge in this LED is –76 meV. The unusual energy redshift can be explained by carrier relaxation [67]. As the temperature is decreased, the carrier lifetime increases due to reduced nonradiative rates, allowing more opportunity for carriers to relax into lower-lying localized states. The energy redshift, and therefore the degree of carrier relaxation, decreases as the In content in the active region increases. In the green LED, the peak redshifts by only ~10 meV in the temperature range of 150–250 K and stabilizes at 2.37 eV at lower temperatures. This behavior can be interpreted as evidence of strong localization effects in this LED. A large number of localized states in the MQWs are responsible for efficient carrier capture and recombination over the entire temperature range. In contrast, the UV LED demonstrates different emission mechanisms within different temperature ranges. While localized state recombination appears to be important below 150 K when carriers are transferred to lower-energy states, band-to-band transition becomes dominant at higher temperatures as the localized carriers are thermalized. Indeed, with increasing temperature above 200 K, the EL peak of the UV LED exhibits a redshift, which follows the characteristic temperature dependence of the GaN bandgap shrinkage [68]. The thermal energy at 150 K ~ 13 meV can be estimated as the magnitude of the localization energy in the UV LED.

Figure 1.9 shows the *L*–*I* characteristics of the LEDs measured at 5 K. Light intensity *L* is linear with current *I* in the low injection regime for all devices, indicating dominant radiative recombination and a constant quantum efficiency. As current increases, the light output shows a trend of saturation. The dependence of light output on forward current becomes sublinear in the high injection regime,

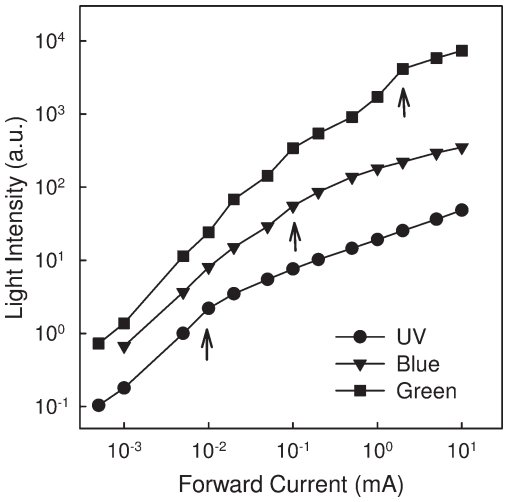

Fig. 1.9 The *L–I* characteristics of InGaN/GaN MQW LEDs at 5 K. The arrows indicate the current levels where the light output tends to saturate.

following $L \sim I^m$ ($m \sim 0.4$). The transition point where the EL intensity tends to saturate moves to higher injection currents as the In content increases. This is evidence that carrier capture becomes inefficient at low temperatures. In the UV LED, there are only a limited number of localized states, and therefore only a small portion of the injected carriers can transfer to localized states, whereas a significant number of carriers may escape from the InGaN QWs. As expected, there are a large number of localized states in the green LED, offering carriers more opportunities to be captured. The *L–I* data can be fitted to the solution of the rate equation, which describes carrier capture and decapture processes in the MQWs at steady state:

$$\frac{dN}{dt} = (N_0 - N) j_c \sigma_{cap} - N\left(\frac{1}{\tau_{decap}} + \frac{1}{\tau_{rad}} + \frac{1}{\tau_{nonrad}}\right) = 0 \tag{1.6}$$

where N_0 is the total number of localized states, N is the number of captured carriers, j_c is the flux of carrier injection, σ_{cap} is the effective cross-section for carrier capture, and τ_{decap}, τ_{rad} and τ_{nonrad} represent the lifetimes associated with carrier decapture, radiative and nonradiative recombination, respectively. Considering that the nonradiative lifetime of localized carriers τ_{nonrad} and the carrier decapture time τ_{decap} at low temperatures (<150 K) are quite long, and that the EL intensity L is proportional to N/τ_{rad}, we obtain

$$L = \frac{N_0}{(1/j_c\sigma_{cap}) + \tau_{rad}} \tag{1.7}$$

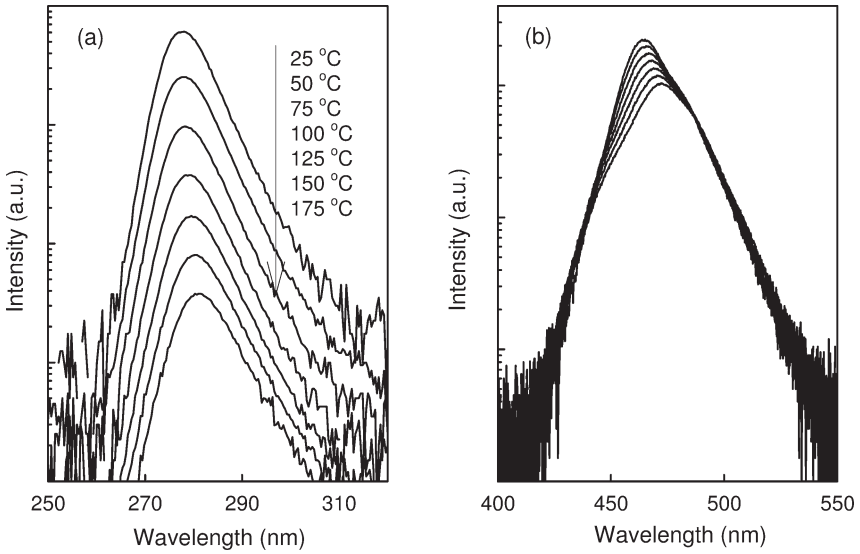

Fig. 1.10 Temperature-dependent EL spectra of (a) a deep-UV LED and (b) a blue LED at 10 mA.

From Eq. (1.7), L is given by $L = N_0 j_c \sigma_{cap}$ in the limit of $j_c \to 0$. On the other hand, L saturates to the value of N_0/τ_{rad} at high currents ($j_c \to \infty$). The radiative decay time is expected to be longer in the green LED due to the larger size of QD structures [69]. The output power of the green LED at high currents (>10 mA) is ~200 times higher than that of the UV LED, as shown in Fig. 1.9, suggesting that the density of the related localized states in the green LED is more than two orders of magnitude higher.

The localization effects also have a significant impact on the LED performance at elevated temperatures. Figure 1.10 illustrates the evolution of the EL spectra of a deep-UV (280 nm) LED and blue (465 nm) LED with increasing temperature. As temperature is increased from 25 °C to 175 °C, the emission of the UV LED shows a much sharper decrease, by a factor of 48, compared to only a 42% decrease for the blue LED. While the high-energy side of the blue LED spectra shows a slow decrease in emission intensity, the intensity and energy of the low-energy band, especially the tail, are almost temperature-independent. The low-energy emission is dominated by emission at localized states and less sensitive to the change in temperature. The localization effects remain strong even at 175 °C, as also revealed by a blueshift of the EL peak with increasing current, suggesting a localization energy >39 meV. A previous study using time-resolved photoluminescence (TRPL) showed that the localization energy in an InGaN material with a composition similar to the blue LED QWs was ~60 meV [70], corresponding to an indium compositional fluctuation of ~0.03. As a contrast, the low-energy and high-energy sides of the UV emission spectra exhibit similar temperature dependence of

emission intensity and energy. The redshift of the UV peak follows the temperature dependence of the AlGaN bandgap as described by Varshni's equation

$$E_g(T) = E_g(0\,\mathrm{K}) + \alpha T^2/(T-\beta) \tag{1.8}$$

with values $\alpha = 5.08 \times 10^{-4}\,\mathrm{eV\,K^{-1}}$ and $\beta = 996\,\mathrm{K}$ [71]. These behaviors again suggest minimal localization effects in AlGaN alloys and that the UV emission is dominated by band-to-band transition. The much sharper decrease in EL intensity of the UV LED compared to the blue LED is due largely to its shallower AlGaN QWs and a higher defect density in the active region. The band offset between the well/barrier layers is ~0.28 eV in the UV LED, much smaller than ~0.71 eV in the blue LED. The above results also suggest that the lack of localization effects in AlGaN is another causal factor in the poor thermal performance of the UV LED, and that increasing carrier confining potentials will provide a critical means to improve UV LED performance.

1.2.5 Radiative and Nonradiative Recombination

The MQW structure greatly enhances carrier confinement and radiative recombination rates. However, nonradiative recombination can never be totally eliminated. Injected carriers may recombine nonradiatively through defect states in the QWs or escape from the QWs via tunneling or thermal motion and then recombine through defect states in the barrier and cladding layers. The unique material properties of InGaN, including strong localization effects and a large exciton binding energy, distinguish the radiative and nonradiative processes from other III–V materials. In high-quality blue and green LEDs, most carriers are captured by localized states in the QWs, leading to a dominant radiative process with an efficiency as high as 70–80%. With decreasing In content in the active region, the density of localized states decreases, and carriers have more chance to be captured by defect states. It has been demonstrated that the quantum efficiency of nitride LEDs decreases dramatically when the emission wavelength is shorter than 380 nm [72]. Particularly in AlGaN-based deep-UV LEDs, the radiative and nonradiative decay times are strongly affected by the presence of microstructural defects and polarization charge-induced field. The highest external quantum efficiency of 280 nm LEDs reported to date is less than 2% [2].

While most recombination processes via defect states are nonradiative, some deep-level transitions are radiative. Figure 1.11 shows current-dependent EL spectra of a blue LED whose *I–V* characteristics are dominated by carrier tunneling [see LED B in Fig. 1.5(a)]. At currents less than 0.02 mA (forward voltage <2.5 V), a broad deep-level emission centered at ~550 nm dominates. With increasing current, the QW emission at 460 nm increases rapidly, whereas the deep-level emission tends to saturate, suggesting that the yellow defect luminescence and carrier tunneling may be associated with the same prominent defect states in the

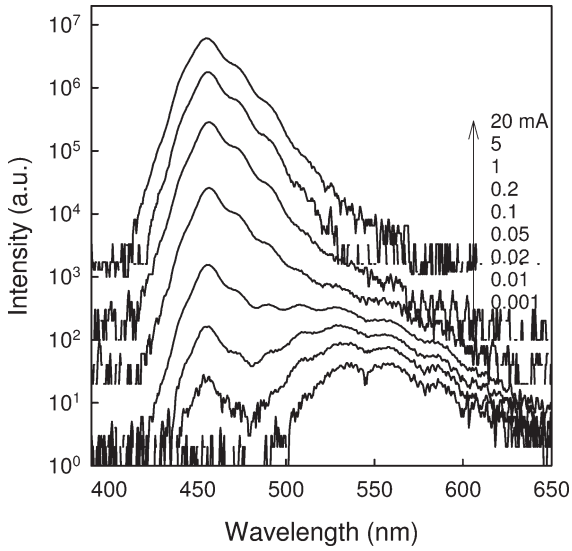

Fig. 1.11 Current-dependent EL spectra of an InGaN/GaN MQW blue LED.

space-charge region. Much stronger defect emission is usually observed in AlGaN UV LEDs [18, 73–75], where the defect state density is higher. Zhang et al. [76] reported a 280 nm LED with a defect emission band at ~320 nm, which was attributed to transitions involving deep acceptor levels in the p-type cladding layer. By increasing the carrier confinement potential, the ratio of QW and defect emission intensities at 20 mA was improved from 1.5 : 1 to 47 : 1.

The *L*–*I* characteristics of a LED in a specific injection regime can be fitted with a power law, $L \propto I^m$. The parameter m reflects the influence of defect states on carrier recombination processes [77]. As nonradiative recombination dominates, L shows a superlinear dependence on I ($m > 1$). In this case, the internal quantum efficiency increases with increasing current. When defect states are saturated and radiative recombination becomes dominant, a linear increase of L with I ($m \sim 1$) can be expected. The quantum efficiency becomes a constant. Figure 1.12 shows the *L*–*I* characteristics of an InGaN/GaN MQW UV LED measured at 5 K, 77 K, 150 K, and 300 K. The light output varies as I^2 at 300 K, indicating a significant influence of defects even at high current densities. At 150 K, even though some defects are frozen out, the impact of the defect states is still clearly seen at low currents (less than 0.1 mA). As temperature is further decreased, the transition point from nonradiative recombination to radiative recombination moves to lower injection currents. In high-quality blue and green LEDs, a linear relationship between L and I can be obtained in all injection regimes at room temperature [78], implying a much smaller role of defect states.

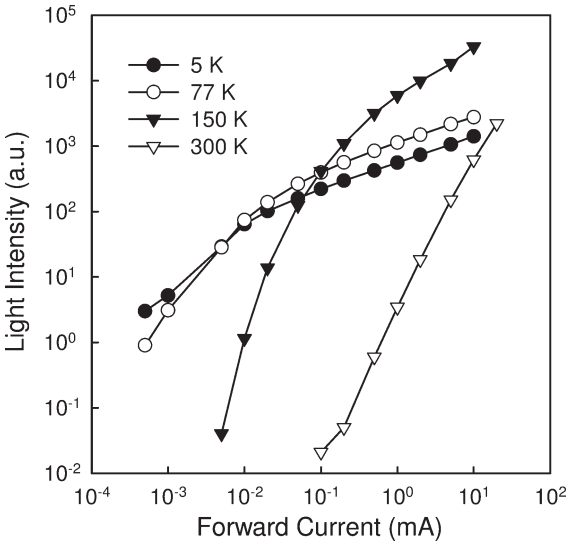

Fig. 1.12 The *L–I* characteristics of an InGaN/GaN MQW UV LED measured at 5 K, 77 K, 150 K, and 300 K.

1.2.6 Light Extraction

For LEDs having a quantum efficiency of unity, the recombination of every electron–hole pair generates one photon in the active region. The photons must escape from the semiconductor material in order to contribute to the total light emission. Just as with conventional III–V LEDs, light trapping inside LED chips is a primary limitation for producing efficient III–nitride LEDs. The large contrast in index of refraction between nitrides and the surrounding media gives rise to a small critical angle for total internal reflection as determined by Snell's law, and small light escape cones. A large portion of the generated light is trapped and rattles around until it is absorbed by the semiconductor, substrate or contact metals. The refractive index of GaN is ~2.5 at blue wavelengths, much larger than that of sapphire ($n = 1.78$) and a typical epoxy ($n = 1.5$). For LEDs grown on sapphire, light outside the escape cones is trapped within the thin epilayer. Based on ray-tracing simulation, we have found that the extraction efficiency of a planar blue LED on sapphire is about 12% without encapsulation, and about 27% with epoxy encapsulation.

In top-emitting LEDs, a significant amount of light is absorbed by the bondpads, semitransparent p-contact, and die-attach material. This type of loss can be prevented by employing a reflective p-type metal contact and a flipchip bonding scheme [79, 80]. In this case, the LED is flipchip mounted either on a submount or directly on a printed circuit board using an eutectic melt process, as illustrated in Fig. 1.13(a). All light is extracted through the transparent sapphire substrate. The flipchip configuration thus has a higher light extraction efficiency and is par-

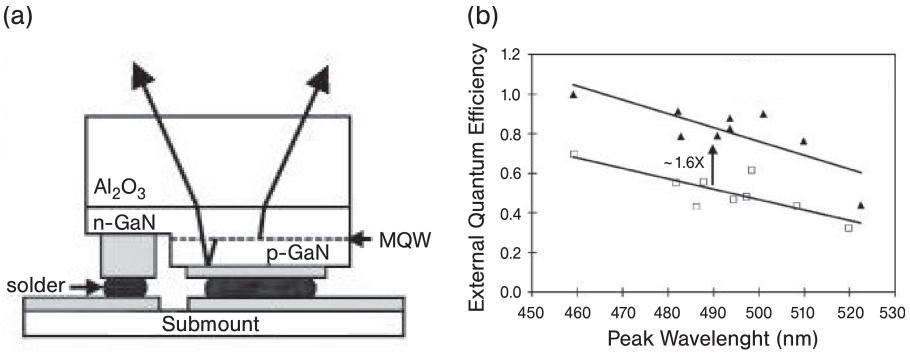

Fig. 1.13 (a) Schematic cross-section of an InGaN/GaN flipchip LED mounted on a submount. (b) Normalized external quantum efficiencies of top-emitting LEDs (open squares) and flipchip LEDs (solid triangles) tested at 350 mA pulse current. After Ref. [79].

ticularly important for developing high-efficiency UV (<370 nm) LEDs because the p-GaN contact layer and p-metal are strongly absorbing in the UV regime. Another advantage of flipchip LEDs over top-emitting LEDs is their superior thermal management. Heat generated in the junction can be removed efficiently through the thick p-metal and solder bumps, overcoming the disadvantage of the poor thermal conductivity of sapphire. Flipchip LEDs therefore suffer less from joule heating and can be driven at much higher currents.

The p-type metallization of flipchip LEDs has three functions: an ohmic contact, a current spreading layer, and an optical reflector. Silver is the metal of choice due to its high reflectivity at wavelengths longer than 400 nm, and its ability to form low-resistance ohmic contacts to p-GaN [80]. The whole metallization typically consists of a multilayer metal stack, including a diffusion barrier layer which prevents Ag from electromigration, and a solder layer for subsequent die attachment. Aluminum has a reflectivity greater than 90% at visible wavelengths, and thus can be utilized to form reflective n-type contacts. Figure 1.13(b) shows a plot of normalized external quantum efficiencies of top-emitting LEDs and flipchip LEDs tested at a 350 mA pulse current [79]. The LEDs with the same emission wavelengths were fabricated from the same epitaxial wafer. The flipchip LEDs have an external quantum efficiency 1.6 times higher than the top-emitting LEDs, suggesting a 60% increase in light extraction efficiency via flipchip packaging.

Many approaches have been explored to improve light extraction from LEDs on sapphire, including roughening chip surfaces [81, 82], texturing sapphire substrates [83, 84], integrating LEDs with a sapphire microlens [85] or photonic crystals [86, 87], and utilizing surface plasmon resonance [88]. The philosophy common to the first three approaches is to deliberately redirect the waveguided light, reduce total internal reflection, and consequently induce light emission in off-plane directions. Providing that the majority of the light is trapped inside the nitride film,

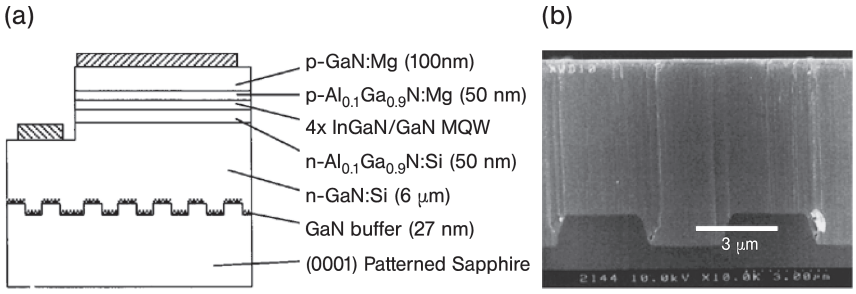

Fig. 1.14 (a) Schematic diagram and (b) SEM cross-sectional micrograph of a 382 nm InGaN/GaN MQW LED grown on a patterned sapphire substrate. After Ref. [83].

one of the most effective ways is to texture the sapphire surface to suppress the guided modes. Figure 1.14 depicts a schematic diagram and scanning electron microscope (SEM) cross-sectional micrograph of a 382 nm InGaN/GaN MQW LED grown on a patterned sapphire substrate [83]. Parallel grooves were fabricated using standard photolithography and subsequent reactive ion etching along the $\langle 11\bar{2}0 \rangle$ direction. The flipchip-mounted LEDs exhibited an output power of 15.6 mW and an external quantum efficiency of 24% at 20 mA. The improved efficiency is a result of enhanced light extraction through the sapphire substrate as well as improved material quality yielded by lateral growth on the patterned substrate.

1.3 LEDs on SiC Substrates

SiC has also been used as a growth substrate for high-brightness InGaN-based LEDs [89, 90]. One main advantage of using SiC is that it can be easily doped to make a conductive substrate, enabling the fabrication of LEDs with a vertical geometry, similar to conventional III–V LEDs grown on conductive GaAs and GaP substrates. Nonuniform current spreading, as exists in lateral LEDs on sapphire, is therefore mitigated. The fabrication and packaging of such a LED chip is relatively straightforward, as a mesa structure is not needed. A Ni-based contact is formed on the backside of the substrate as the n-type electrode, and only one wire bond is required for top-emitting LEDs. SiC also has the advantage of being highly thermally conductive. Its thermal conductivity is ~10 times higher than that of sapphire, greatly enhancing heat removal from LED chips. Additionally, unlike sapphire, SiC has natural orthogonal cleavage planes, which facilitate the chip separation process. The cleavage planes are particularly important for producing high-quality facets to form resonant cavities in laser diodes (LDs).

Using SiC substrates for III–nitride LEDs, however, is less common mainly due to their high cost. Even though SiC has a smaller lattice mismatch (~3.5%) with GaN than sapphire, it is sufficiently large to result in a large number of disloca-

tions (10^8–10^{10} cm^{-2}) in epilayers [91–93]. As compared to sapphire wafers, epi-ready SiC wafers typically have a rougher surface finish and a larger number of surface and bulk defects, which are additional sources of microstructural defects in epilayers. Another drawback is that doped SiC is typically opaque at the wavelengths of visible light. It is strongly absorbing at UV wavelengths shorter than its band-edge emission (~410 nm for 6H-SiC) and is not suitable for developing high-efficiency deep-UV emitters.

GaN epilayers are usually grown on the (0001) plane of Si-face 6H- or 4H-SiC substrates using the MOCVD technique. An AlN or AlGaN buffer layer is required to help accommodate the lattice mismatch and relieve stress. AlN can nucleate on SiC at both low and high temperatures [91–93]. In contrast to low-temperature buffer layers on sapphire, AlN deposited on SiC at high temperatures (~1100 °C) has better crystalline quality and surface morphology [92], and therefore it is more effective for promoting subsequent 2D growth of high-quality films. Because SiC has a smaller thermal expansion coefficient, upon cooling down from the growth temperature GaN epilayers may be under a tensile stress, which favors the formation of cracks. It has been suggested that the strain state of GaN epilayers is determined by their growth mode, and tensile strain can be avoided by growing GaN on a thin coherently strained AlN buffer layer [94].

Cree's first-generation InGaN-based blue LEDs employed a highly-resistive AlN buffer layer [89]. To bypass this resistive layer, a shorting ring was employed that allowed vertical flow from the LED structure to the SiC substrate. The AlN buffer was later replaced by a Si-doped low-Al content AlGaN layer [89], which is conductive but may still introduce a significant series resistance. State-of-the-art blue and green LEDs grown on SiC have a layer structure similar to those grown on sapphire, and are comparable in microstructural quality, electrical properties, and optical characteristics.

SiC has a refractive index (~2.7 at blue wavelengths) slightly higher than GaN, but considerably higher than epoxy. No total internal reflection occurs at the GaN/SiC interface. Thus, in LEDs with a rectangular geometry, most light emitted by the active region is trapped inside the SiC substrate and has a good chance to be absorbed by the substrate and bottom contact. Chip shaping and texturing are, therefore, critical for light extraction. A truncated inverted pyramid (TIP) LED is an example of chip shaping of an individual LED [95] that is achieved by dicing a chip with a beveled blade to yield a sidewall angle in the range of 30°–50° with respect to the vertical. Such a shape enhances light extraction by redirecting the internally reflected light and reducing the average light path within the chip, as illustrated in Fig. 1.15(a). Figure 1.15(b) shows the calculated light extraction efficiency of a blue LED on SiC as a function of the sidewall angle. An absorption coefficient of 5 cm^{-1} was used for the SiC substrate. With an angle ~35°, light extraction can be increased by 110% compared to a rectangular chip. Cree's XB LEDs employ this chip shaping technique [see Fig. 1.15(c)] in conjunction with flipchip packaging, providing a record performance with an external quantum efficiency of ~45% at 450–455 nm, corresponding to a radiant power of 25 mW at 20 mA [96].

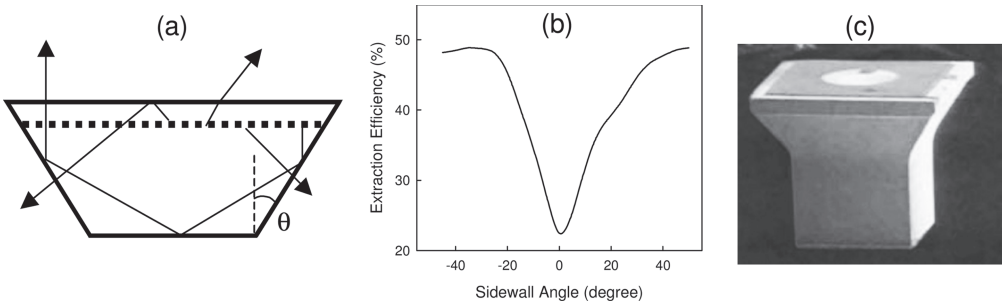

Fig. 1.15 (a) Schematic diagram of a TIP LED illustrating the enhanced light extraction efficiency. (b) Calculated light extraction efficiency of a blue LED on SiC as a function of the sidewall angle. (c) A shaped Cree LED chip.

1.4 LEDs on Si Substrates

The allure of low-cost light sources has fueled a variety of efforts to grow III–nitride LEDs on Si substrates [97–103]. Si is thermally stable under typical nitride growth conditions. Si wafers, with high crystalline quality and a smooth surface finish, are available in large sizes at low prices. Using Si substrates allows easy die separation, simple wet-etch substrate removal, and the potential to integrate LEDs with Si control electronics.

III–nitride blue and UV LEDs have been grown on Si(111) using molecular-beam epitaxy (MBE) [97, 98] and MOCVD [99–103]. The enormous 17% lattice mismatch of GaN on Si mandates the use of a buffer layer such as AlN or AlGaN [97–108]. Besides reducing crystalline defects, the buffer layer also enhances 2D growth of GaN and prevents the formation of an amorphous SiN_x interlayer [105]. The greater thermal expansion coefficient of GaN as compared to that of Si gives rise to a tensile stress in epilayers. Cracking may occur upon cooling down from the growth temperature [99]. The cracking problem may be reduced by optimizing the structure and growth of the buffer layer. It was recently found that MOCVD-grown GaN epilayers on a thick AlN–GaN graded buffer were under a compressive stress and free of cracks [106]. Both a step-graded AlGaN buffer and an AlN/GaN superlattice have also proven to be effective for reducing the crack density [107, 108]. Most recently, by employing a high-quality AlN buffer layer, Li et al. [103] successfully scaled blue LEDs on Si wafers up to 6 inches.

LEDs grown on Si are fabricated in a similar fashion to LEDs on SiC by forming the n-type contact on the backside of the substrate and have a vertical structure, which greatly enhances current spreading uniformity. However, most reported LEDs on Si have a high series resistance, due to the large band offset between the AlN buffer and Si substrate, as well as poor doping in the p-type cladding layer [99, 102]. Despite the use of an AlN buffer layer, the crystalline quality of epilayers on Si cannot be compared to those obtained on sapphire. State-of-the-art LEDs on Si are at least 10 times less efficient than their counterparts on sapphire or SiC

substrates. The highest reported performance is still sub-milliwatt output power at 20 mA and less than 1% external quantum efficiency [100]. The LED performance is fundamentally limited by two key factors: poor light extraction due to the inherent visible and UV light absorption of silicon, and high defect density due to the aforementioned high thermal and lattice mismatch between Si and nitrides. Nevertheless, with a significant cost reduction possible from 6 inch Si wafers, these LEDs hold promise for special applications where high brightness is not required.

Light absorption by the substrate results in a significant light loss in LEDs grown on Si wafers. One way to reduce this parasitic loss is to insert an AlGaN/GaN distributed Bragg reflector (DBR) between the LED structure and the Si substrate [101]. The DBR, however, will increase the operation voltage and substantially increase the possibility of film cracking. Another way is to remove the Si substrate and transfer the LED film to a reflective substrate. A similar approach has been employed to improve heat dissipation and light extraction of blue LEDs on sapphire [109–110]. In this case, the separation was realized using a laser lift-off technique due to the chemical inertness of sapphire. Si can be readily removed by selective chemical wet etching. The substrate removal can not only greatly improve the light extraction efficiency but also eliminate the conduction barrier at the buffer/Si interface. Zhang et al. [102] reported the separation of an InGaN MQW green LED from Si and transfer to a copper carrier. The LED wafer with an Al/Au metal reflector deposited on the p-contact was first bonded onto an Au plating copper carrier using indium. The Si substrate was thinned down to 60 μm and selectively etched in a $HF:HNO_3:CH_3OOH$ (1:1:1) solution. The AlN/AlGaN buffer layer was then plasma etched, and the n-type electrode, which consists of a Ti/Au (5 nm/5 nm) semitransparent contact and an Al/Au bondpad, was formed on the exposed n-GaN layer. Figure 1.16 shows the *I–V* and *L–I* characteristics of the LED before and after this process. The series resistance was reduced from 42 Ω to 27 Ω, and the optical power was increased by 49%. Further improvement in light extraction can be expected by using a more transparent n-type contact and an appropriate encapsulation.

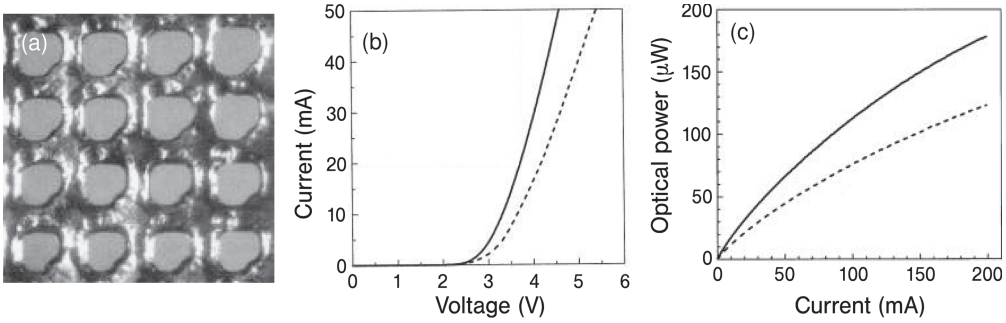

Fig. 1.16 (a) SEM image of a green LED after partial removal of the Si substrate. (b) The *I–V* characteristics and (c) the *L–I* characteristics of the LED before (dashed line) and after (solid line) substrate removal. After Ref. [102].

1.5 LEDs on Free-Standing GaN Substrates

For LEDs grown on foreign substrates, the mismatches in lattice constant and thermal expansion coefficient between the nitrides and substrates manifest themselves as a high density of threading dislocations and residual biaxial stress in the epilayers. High-quality bulk GaN substrates, if available, would significantly mitigate these problems. The growth procedure for GaN-based LEDs can be greatly simplified as the homoepitaxy process does not require additional steps, such as surface nitridation and low-temperature buffer layer, which are mandatory in heteroepitaxial growth. The defects and stress in the epilayers would be greatly reduced, leading to improved performance, yields, and scalability to larger substrates. In addition, simple vertically structured LEDs can be fabricated on conducting GaN substrates. The vertical geometry, in combination with good thermal conductivity of GaN (5× higher than sapphire), allows the LEDs to operate at much higher current densities and temperatures.

1.5.1 LED Homoepitaxy

The chemical passivity of nitrogen, and the high melting temperature and high decomposition pressure of GaN have made growth of large-size and high-quality GaN boules problematic. A number of bulk GaN crystal solution growth techniques are under development [111–115], which use liquid gallium or gallium alloys as a solvent and a high pressure of nitrogen above the melt to maintain GaN as a thermodynamically stable phase. One of the most intensively explored approaches is high-pressure solution growth (HPSG) developed by Porowski et al. [111, 112]. Bulk GaN crystals are grown from a Ga melt, under a nitrogen hydrostatic pressure of about 15 kbar at temperatures ranging from 1500 to 1800 K, and crystallize in the form of platelets or rods. The process is capable of growing GaN crystals with a dislocation density lower than $10^4\,cm^{-2}$. The undoped crystals have a high n-type background doping, on the order of $5 \times 10^{19}\,cm^{-3}$, which is believed to be due to oxygen impurities and nitrogen vacancies, which also causes some crystal opacity. One major drawback of such a technique, however, is that the quality of the GaN crystals deteriorates with increasing growth rate and size, thus limiting the maximum crystal size to ~10 mm.

A more mature technology for growing bulk GaN is hydride vapor-phase epitaxy (HVPE) [116–121], which is normally carried out in a hot wall reactor at atmospheric pressure. In this approach, vapor-phase GaCl, formed by reacting HCl with liquid Ga at 800–900 °C, is transported to a substrate, such as sapphire, Si or GaAs, where it reacts with injected NH_3 at 900–1100 °C to form GaN. As compared to other epitaxial growth approaches, much higher growth rates (on the order of $100\,\mu m\,h^{-1}$) can be attainable by HVPE [119], making it a potentially low-cost technique for mass-producing bulk GaN. Free-standing GaN substrates can be produced by separating thick HVPE grown GaN from the underlying substrate using

laser beam radiation or mechanical polishing. Lapping, polishing, and etching are then performed to achieve GaN wafers with an epi-ready surface.

The dislocation density in HVPE-grown GaN films is initially quite high, on the order of $10^{10}\,cm^{-2}$ as is typical for heteroepitaxially grown thin GaN layers. As the epilayer thickness increases, the evolution and annihilation of the dislocations lead to a reduction in dislocation population. The density usually drops to a value of about $10^{7}\,cm^{-2}$ after a thickness of 100–300 µm of GaN has been grown [119]. However, large strain and associated bowing or cracking, which result from the use of a foreign substrate, will limit the maximum film size and thickness. The strain and bowing remain even after removal of the original substrate, and are expected to be also present in epitaxial layers deposited on such substrates. By improving strain management, Xu et al. [120] successfully fabricated 2 inch GaN boules as thick as 10 mm with a dislocation density as low as $10^{4}\,cm^{-2}$. HVPE GaN may also contain a high density of point defects, such as N vacancies and impurities, leading to a high background doping level and a redshift of the emission spectrum.

GaN homoepitaxy using MOCVD is more straightforward than heteroepitaxial growth. The substrate is heated directly to the growth temperature in an ammonia-rich environment. 2D growth mode can be achieved on GaN(0001) without using a buffer layer. Homoepitaxially grown GaN usually shows a smooth surface with a step structure, in contrast to a swirled step structure for typical epitaxy on sapphire. It has been found that vicinal surfaces with an offcut of 1–2 degrees yielded smoother morphology than nominal *c*-plane [121]. This can be understood by the fact that the offcut surfaces provide predefined atomic steps for smooth 2D step-flow growth. Homoepitaxial GaN, in most cases, replicates the defect structure in the bulk substrates [122]. However, surface defects introduced in the polishing and etching steps were found to have a pronounced impact on the homoepitaxial quality [123] and must be removed by additional chemomechanical polishing or chemically assisted ion-beam etching. Figure 1.17 shows high-resolution X-ray diffraction (HRXRD) rocking curves of the (0002) reflection of an HVPE GaN substrate, and GaN epilayers grown atop the substrate and sapphire. The FWHM of the homoepitaxial GaN is 79 arcsec, which is comparable to that of the substrate (85 arcsec), but much smaller than for the heteroepitaxial GaN (230 arcsec). Since the FWHM of the (0002) peak reflects the degree of lattice distortion from dislocations, the smaller FWHM of the homoepitaxial GaN confirms that the threading dislocation density is substantially reduced. Our recent study showed that the incorporation of common impurities in homoepitaxial GaN, including C, H and O, was significantly reduced compared to GaN grown on sapphire [124]. This may be a result of dislocation reduction in the homoepitaxial GaN as impurities tend to congregate around microstructural defects and create localized states in the bandgap [125].

The growth of III–nitride LEDs on bulk GaN substrates is referred to here as homoepitaxy even though the alloy composition and lattice constants of the active and cladding layers may not be identical to those of the substrate. While visible LEDs with GaN cladding layers are well matched to the substrate and slightly

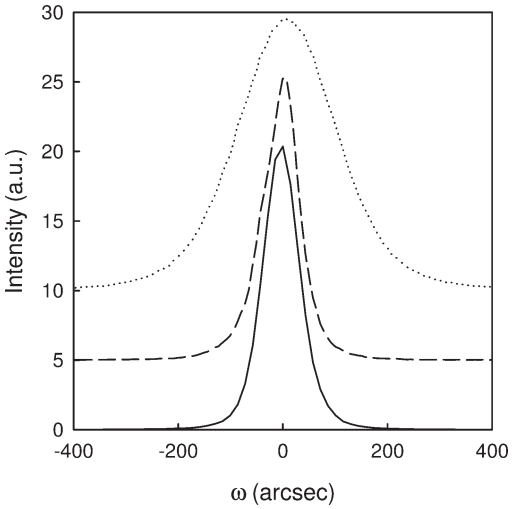

Fig. 1.17 HRXRD rocking curves of the (0002) reflection from an HVPE GaN substrate (solid line) and GaN epilayers grown on bulk GaN (dashed line) and sapphire (dotted line).

strained, UV LEDs based on AlGaN heterostructures grown on bulk GaN may suffer from a large tensile stress, thus causing cracks. An additional stress-relief layer, such as a graded AlGaN layer, is required for growing thick LED structures.

Pelzmann et al. [126] reported the growth of homojunction GaN LEDs by depositing a p-GaN layer on an n-type HPSG GaN substrate. The homoepitaxial LEDs demonstrated a doubling of the emission intensity relative to their counterparts on sapphire. Franssen et al. [127] studied the electrical and optical characteristics of HVPE-grown InGaN/GaN MQW blue LEDs on a similar GaN substrate. Thermionic emission rather than tunneling transport was found to be the main mechanism responsible for radiative recombination in the LEDs. The maximum internal and external quantum efficiencies were determined to be 38% and 1.9%, respectively.

We have investigated the growth of InGaN/GaN MQW LEDs on free-standing HVPE GaN substrates using low-pressure MOCVD. The GaN substrates, offcut by 1–2 degrees in the $\langle 11\bar{2}0 \rangle$ direction, were ~300 μm thick, unintentionally doped, and had a free carrier concentration of $\sim 7 \times 10^{17}\,\mathrm{cm}^{-3}$. Atomic force microscopy (AFM) measurement showed that threading dislocations were terminated by surface pits after the chemomechanical polish and the density was determined to be $\sim(1\text{–}2) \times 10^{7}\,\mathrm{cm}^{-2}$. The substrates were heated directly to 1050 °C in a steady ammonia flow, followed by the growth of the n-GaN cladding layer. The growth recipes for subsequent InGaN QWs and AlGaN layer were similar to those known for heteroepitaxial LEDs. The active regions were 10-period InGaN/GaN MQWs with an In composition ranging from 0.1 to 0.21.

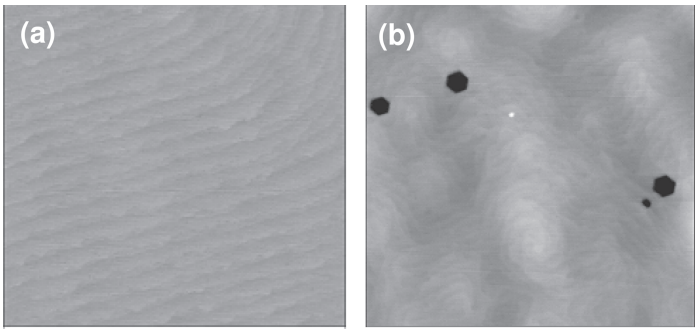

Fig. 1.18 AFM images (2 μm × 2 μm) of InGaN/GaN MQW LEDs grown on (a) GaN and (b) sapphire.

Figure 1.18(a) shows a 2 μm × 2 μm AFM image of the homoepitaxial LED. The surface is defect-free, and a step structure with terraces of ~100 nm is clearly seen. In contrast, a similar structure grown in the same epitaxy run on sapphire with a previously grown buffer exhibits a rougher morphology and ~1 × 10^8 cm^{-2} V-defects ranging from 50 to 150 nm [see Fig. 1.18(b)]. The rms roughness of the LEDs on GaN and sapphire are 0.23 nm and 0.65 nm, respectively. The smooth surface of the homoepitaxial LED suggests abrupt heterostructural interfaces and uniform QWs resulted from 2D step-flow epitaxy. The V-defects, which are open hexagonal inverted pyramids defined by six $\{10\bar{1}1\}$ planes, are connected to threading dislocations mostly with screw and mixed character [128]. Microstructural defects and residual stress, which promote the formation of V-defects, are substantially reduced in the homoepitaxial LED. We have found that the growth temperature for the LED on GaN was slightly higher at the same epitaxy conditions, presumably due to the higher thermal conductivity of the substrate. This may partly account for the suppression of V-defects by enhancing the rates of Ga diffusion and incorporation on the off-axis facets [26, 129]. Cross-sectional TEM measurements showed that the density of threading dislocations reaching the active region in the LED on sapphire was ~2 × 10^9 cm^{-2}, whereas it was much lower in the homoepitaxial LED and could not be precisely determined.

1.5.2 Electrical Characteristics

In contrast to lateral LEDs fabricated on sapphire, the LEDs on GaN, with their n-contact formed on the backside of the substrate, have a vertical structure. Figure 1.19 compares the forward *I–V* characteristics of two representative LEDs at various temperatures. As expected, the LED on sapphire shows a characteristic tunneling behavior in the forward direction. Two main exponential segments with different slopes are distinguished at low and moderate forward biases, and can be described by Eq. (1.4). The energy parameter *E*, which is temperature-insensitive,

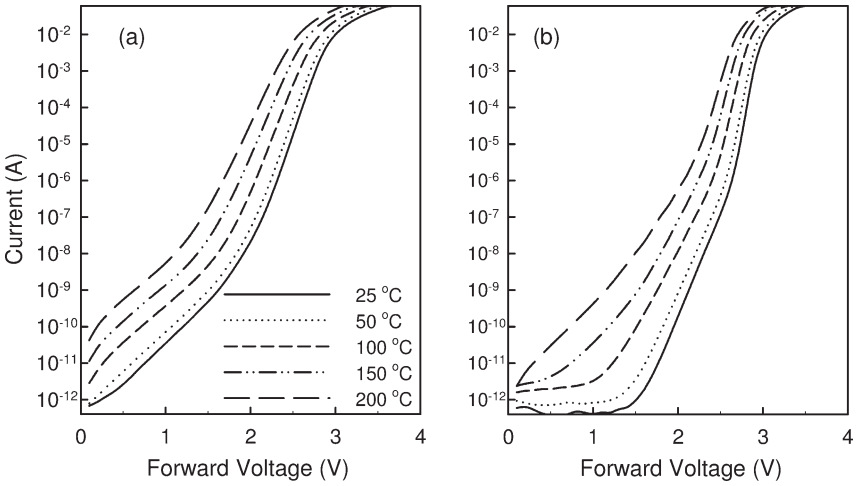

Fig. 1.19 Temperature-dependent forward *I–V* characteristics of InGaN/GaN MQW LEDs grown on (a) sapphire and (b) GaN.

has a value of 190 meV at 0–2.0 V and 70 meV at 2.0–2.8 V. No realistic ideality factors can be extracted. The forward *I–V* characteristics of the LED on GaN, as seen in Fig. 1.19(b), also divide into two distinct linear sections with different slopes, which, however, appear to be a function of temperature. Tunneling may still dominate at low injection levels, but the slope change suggests the involvement of a thermally activated current. As the forward current increases, diffusion and recombination currents start to dominate over the tunneling component. The forward current at bias >2.6 V can be described by Eq. (1.3) with an ideality factor $n = 1.5$ until series resistance in the diode dominates. The presence of the diffusion–recombination currents reflects the high material quality of the homoepitaxial LED, where defect-assisted tunneling current is greatly suppressed.

Carrier tunneling is also seen in the LED on sapphire under reverse bias, as suggested by the strong field dependence but low temperature sensitivity of the reverse leakage current shown in Fig. 1.20(a). In contrast, the LED on GaN shows a dramatic reduction in reverse current by more than six orders of magnitude (Fig. 1.20(b)). The remaining leakage current is a function of both applied bias and temperature, suggesting the coexistence of tunneling and thermal generation currents [45]. In particular, as temperature increases from 100 to 150 °C, there is a sudden jump in the low-bias current, probably arising from thermal ionization of carriers from deep traps and a trap-assisted tunneling process. An activation energy of ~0.6 eV is extracted from the $\log I$ versus $1/T$ plot at −12.5 V where the temperature dependence of the current is roughly an exponential function.

To investigate the microstructural origin of the observed difference in the electrical characteristics of the LEDs, the unmetalized portion of the sample surface was characterized using AFM and conductive AFM (C-AFM). Data were collected

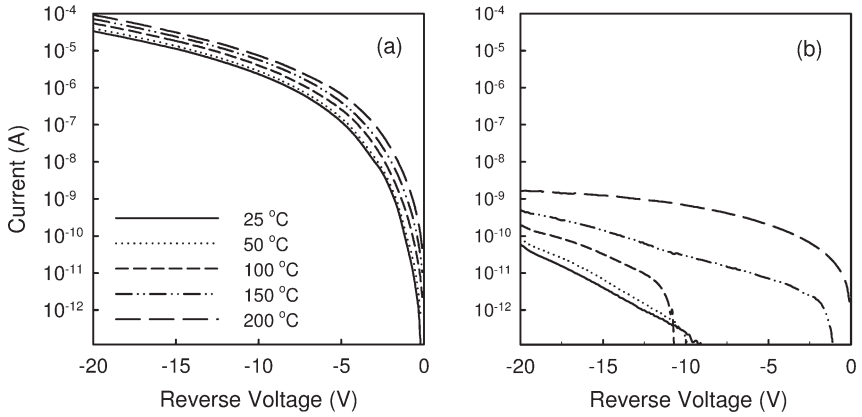

Fig. 1.20 Temperature-dependent reverse *I–V* characteristics of InGaN/GaN MQW LEDs grown on (a) sapphire and (b) GaN.

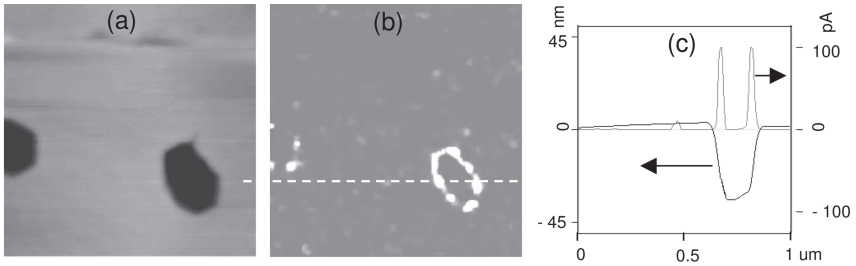

Fig. 1.21 (a) AFM and (b) C-AFM (at −3 V) images (1 µm × 1 µm) of an InGaN/GaN MQW LED on sapphire. (c) Dual section profile taken along the dashed line indicated in (b). The gray scales are (a) 10 nm and (b) 100 pA. The positive current in (c) corresponds to a reverse-bias current in the LED.

under ambient conditions using a conducting diamond-coated tip on a Veeco Instruments Dimension 3000 microscope. A positive or negative bias was applied to the n-type ohmic contact, while holding the tip at ground potential in contact to the topmost p-GaN layer to map the surface current flowing through the junction [128]. The topography of the p-GaN was recorded simultaneously.

The surface of the homoepitaxial LED is free of defects and no current was detected in this sample within the detection limit of our C-AFM system. Figures 1.21(a) and (b) show the topography and current maps of the heteroepitaxial LED over a $1 \times 1\,\mu m^2$ area. The C-AFM current image recorded at −3 V reverse bias (applying a +3 V voltage to the n-ohmic contact) reveals nanoscopic conductivity of the LED structure on sapphire, which correlates well with the topography image. It is striking that the leakage current is highly localized at the edge of the V-defects.

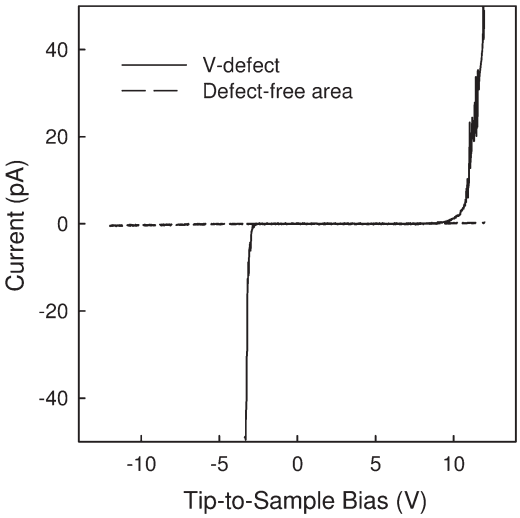

Fig. 1.22 Nanoscale local *I–V* characteristics of an InGaN/GaN MQW LED on sapphire recorded at a V-defect and in a defect-free region.

A dual section profile [Fig. 1.21(c)] shows that the current value is ~100 pA, which corresponds to a current density of ~10 A cm^{-2}. The current scan was repeatable at the same defect, indicating that there was no significant charge accumulation. Increased current conduction was also seen along the edge of the V-defects under forward bias, though the current was much lower. These results are consistent with previous findings that mixed and screw dislocations in GaN are electrically active, creating discrete current paths [130, 131]. It is therefore clear that the V-defects and associated dislocations in the LED on sapphire act as leakage paths connecting the p-GaN and n-GaN layers, and are mainly responsible for the high reverse current observed in this device.

Figure 1.22 presents the nanoscale regional *I–V* characteristics of the LED on sapphire. The data were recorded by placing the diamond tip at a V-defect or at a fixed defect-free region while ramping the bias applied to the n-ohmic contact from +12 V to −12 V. Similar to the case of the homoepitaxial LED, the current in the defect-free region is negligible, whereas the defective area exhibits abrupt turn-on characteristics in both directions. Interestingly, the current rise takes place at a much lower voltage under reverse bias than forward bias. This is because in the latter case the tip behaves as a nanoscale Schottky contact to p-GaN under a reverse bias [132], and therefore the actual voltage dropped on the LED junction may be much smaller than the voltage applied. Given the asymmetric *I–V* characteristics of the reverse-biased nanoscale Schottky contact, the *I–V* curve at the V-defect shown in Fig. 1.22 appears to contain a symmetric current component. Indeed, a similar symmetric leakage current can also be identified near zero bias in Figs. 1.19(a) and 1.20(a). These results support the assumption that the dislocations

associated with the V-defects behave as small shunt resistors connected across the p–n junction.

1.5.3
Optical Characteristics

Figure 1.23 shows a series of EL spectra of near-UV LEDs on GaN and sapphire at different injection levels. The presence of Fabry–Pérot interference fringes is a characteristic feature for LEDs grown on sapphire. As expected, they are absent in the homoepitaxial LED. The peak wavelength of the LED on GaN is 405.5 nm, whereas it is ~5 nm longer on sapphire. This discrepancy may be attributed to the slightly different growth temperatures of the LEDs arising from the difference in substrate thermal conductivity and thermal coupling of the substrates to the susceptors. Neither LED shows a significant blueshift in emission energy with increasing current, as is commonly observed in blue and green LEDs, suggesting weaker localization effects due to a smaller In content. At high currents (>200 mA), the peak wavelength of the LED on sapphire exhibits a redshift as a result of severe joule heating. Another interesting feature shown in Fig. 1.23 is that the spectra of the homoepitaxial LED are narrower (FWHM ~16 nm). This is likely due to smaller composition or thickness fluctuation of the homoepitaxial QWs.

Figure 1.24(a) presents the *L–I* characteristics (on a log–log scale) of the near-UV LEDs measured in continuous-wave (CW) injection mode. The light output of the homoepitaxial LED increases steadily with increasing current, and the dependence

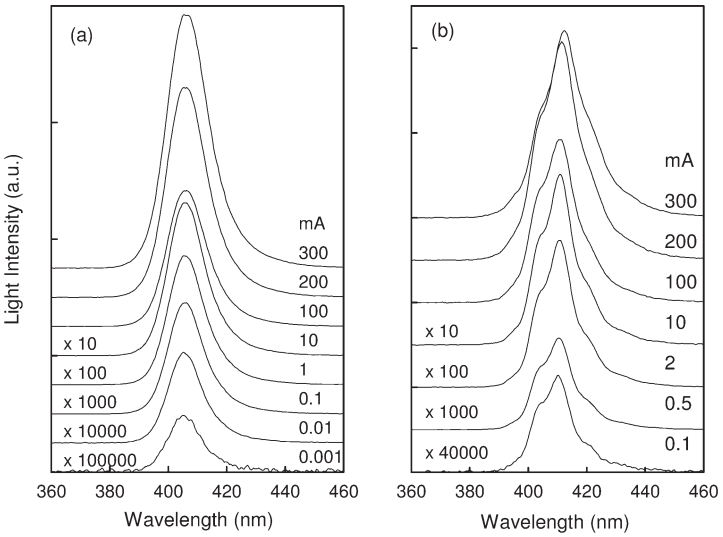

Fig. 1.23 EL spectra of near-UV LEDs on (a) GaN and (b) sapphire at different injection currents.

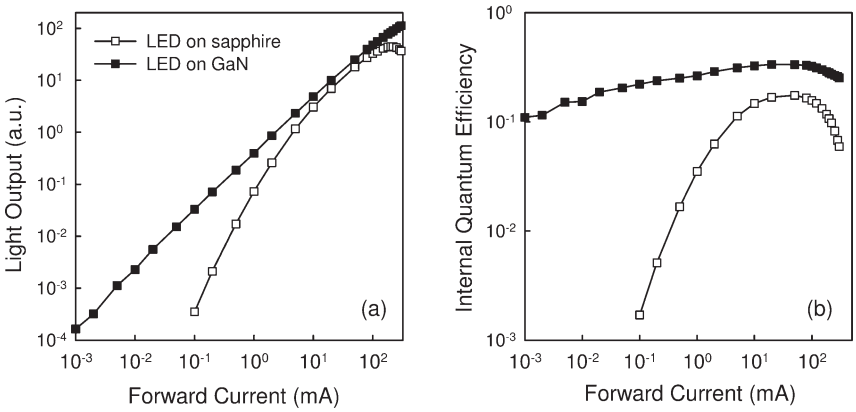

Fig. 1.24 (a) The *L–I* characteristics and (b) calculated internal quantum efficiencies of near-UV LEDs on GaN and sapphire.

is nearly linear over the entire current range. In contrast, the light output of the LED on sapphire shows a superlinear increase at low currents, and a rollover at ~180 mA. At 0.2 mA, 20 mA, and 200 mA, the respective output powers of the LED on GaN are 35×, 56% and 104% higher than the LED on sapphire. The remarkable increase in light emission at low injection levels can be ascribed to a reduced defect density, thus a lower nonradiative recombination rate, as well as enhanced carrier confinement due to higher structural quality of the confining layers. At high currents, the defect states are saturated. The superior performance of the LED on GaN in this case is due largely to the improved current spreading and heat dissipation.

To deduce the internal quantum efficiencies of the LEDs from the measured optical powers, a ray-tracing simulation was performed to determine the light extraction efficiencies. The absorption coefficient of the GaN substrate at 405 nm was found to be ~12 cm^{-1} as determined by transmission measurements, whereas sapphire is essentially transparent. The below-bandgap absorption in the HVPE GaN is caused by a large amount of defects and impurities incorporated during the crystal growth. Like LEDs on SiC, LEDs on GaN have a very small escape cone in all directions due to the high refractive index of GaN ($n \sim 2.5$). As a result, a considerable amount of light generated in the MQWs is trapped and absorbed by the substrate. The calculated chip-to-air light extraction efficiencies of the LEDs on GaN and sapphire at 405 nm are 8.2% and 11.5%, respectively. Taking these into account, the respective increases of the internal quantum efficiency at 0.2 mA, 20 mA and 200 mA are 46×, 103% and 165%. Figure 1.24(b) illustrates the calculated internal quantum efficiency (η_i) of the LEDs as a function of injection current. At low currents, η_i increases rapidly with increasing current as the radiative recombination rate increases. The efficiency of the UV LEDs reaches its maximum value of 33.7% on GaN and 16.8% on sapphire in the current range of

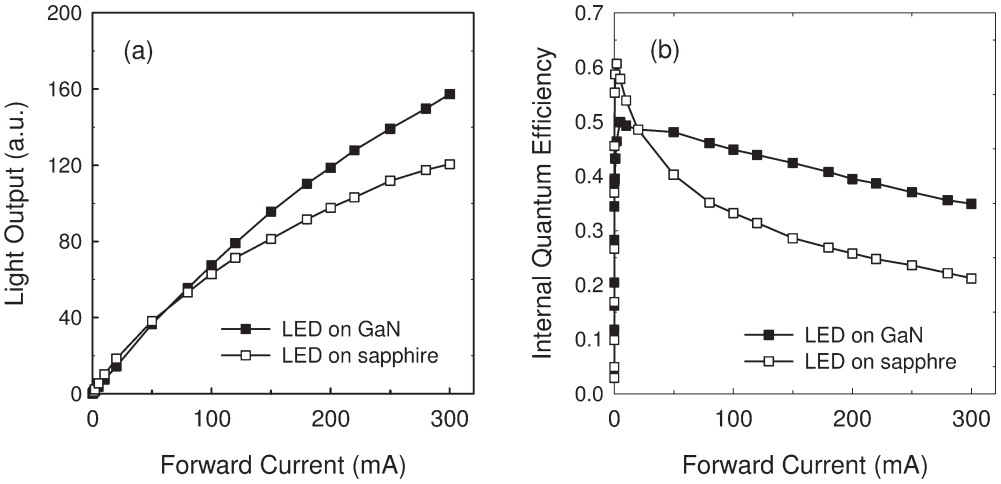

Fig. 1.25 (a) The *L–I* characteristics and (b) calculated internal quantum efficiencies of blue LEDs on GaN and sapphire.

20–50 mA. The peak efficiency of the homoepitaxial LED is expected to be further improved by optimizing its structure design and growth condition. As the current increases further, η_i decreases due to the occurrence of current overflow as the bands are filled up. The efficiency of the homoepitaxial LED decreases at a lower rate at high currents, indicating its suitability for high-power operation.

It is expected, however, that the improvement in material quality, as yielded by homoepitaxy, will have a smaller impact on the optical performance of blue and green LEDs due to stronger localization effects. Figure 1.25(a) compares the *L–I* characteristics of two blue LEDs grown on different substrates. The homoepitaxial LED significantly outperforms its counterpart on sapphire only at high currents (>50 mA), due largely to more efficient heat removal through the GaN substrate. At 20 mA, the light output of the LED on GaN is actually slightly lower than the LED on sapphire. The light extraction efficiencies of the LEDs on GaN and sapphire at 470 nm were calculated to be 9.5% and 12.1%, respectively. The internal quantum efficiencies of the two LEDs at 20 mA are therefore comparable, ~49%, as seen in Fig. 1.25(b). The efficiency of the blue LEDs peaks at a much smaller current of 5 mA as compared to the near-UV LEDs. It then decreases sharply with increasing current for the blue LED on sapphire. This cannot simply be interpreted as a self-heating effect, and may be associated with inefficient carrier capture by localized states due to poor microstructural properties of the heteroepitaxial LED.

As discussed earlier, the performance of AlGaN-based UV LEDs grown on sapphire is limited by poor material quality. Substantial reduction in dislocation density can be achieved by using lattice-matched GaN substrates. It is anticipated that efficient UV LEDs with peak wavelength shorter than 365 nm can be fabri-

cated on bulk GaN despite strong light absorption by the substrate. Nishida et al. [133] demonstrated 352 nm $Al_{0.04}Ga_{0.96}N$ SQW LEDs on a HVPE GaN substrate with 0.55 mW output power and 1% external quantum efficiency at 20 mA. A short-period $Al_{0.16}Ga_{0.84}N/Al_{0.2}Ga_{0.8}N$ superlattice was employed as the transparent p-type cladding layer in the top-emitting LEDs. However, growing thick AlGaN cladding layers on GaN becomes increasingly difficult with increasing Al content due to the lattice and thermal mismatch between AlN and GaN. By using a stress-relief template consisting of 25-period n-type $Al_{0.25}Ga_{0.75}N/Al_{0.2}Ga_{0.8}N$ superlattices with a period of 4 nm, Yasan et al. [134] were able to grow a 340 nm LED structure on a free-standing GaN. The device showed a reduced series resistance and improved output power that is one order of magnitude higher than that of similar LEDs grown on sapphire.

To gain insight into the impact of microstructural defects on the carrier dynamics in AlGaN materials, Garrett et al. [135] performed time-resolved photoluminescence (TRPL) characterization of eight-period $Al_{0.1}Ga_{0.9}N$(3 nm)/$Al_{0.3}Ga_{0.7}N$(7 nm) MQW structures grown on GaN and sapphire substrates. The MQW structure on GaN was fully strained and under a tensile stress. The PL emission centered at 340 nm was four times more intense than from the MQWs on sapphire. Figure 1.26 shows a comparison of TRPL decays for the AlGaN MQWs for the same pump intensity and pump pulse centered at 275 nm. The transient PL for the MQWs grown on sapphire is characterized by a room-temperature lifetime of ~120 ps and a slow decay (~150 ps) that dominates at longer times. The MQWs on GaN exhibit a much longer lifetime, ~500 ps, and a longer slow decay time, ~488 ps. The longer

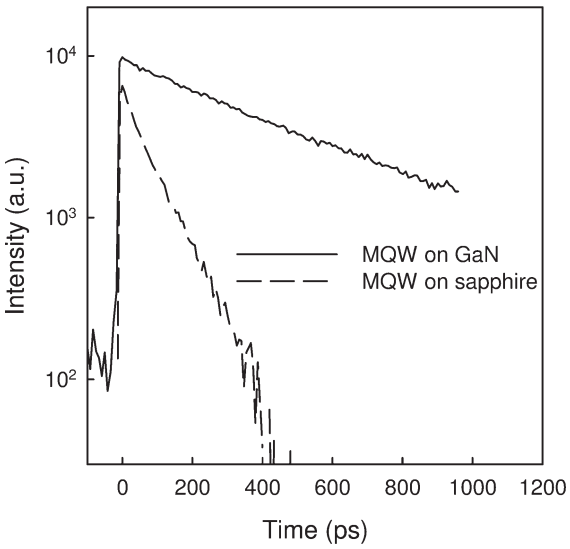

Fig. 1.26 TRPL decay curves at the same pump intensity at 275 nm for $Al_{0.1}GaN/Al_{0.3}GaN$ MQWs grown on GaN and sapphire. After Ref. [135].

PL lifetime of the AlGaN MQWs on GaN reflects better material quality and an increase in nonradiative lifetime associated with the reduction in dislocation density by about two orders of magnitude.

1.5.4
High-Current Operation

In order to compete with fluorescent and other conventional lighting sources, it is essential that the cost of LEDs is further reduced and their efficiency is improved. One way to meet the cost and performance targets is to drive LEDs at much higher current densities without compromising emission efficiency and operating lifetime [136]. III–nitride LEDs grown and fabricated on sapphire are not suitable for high-power operation for several reasons. First, LEDs grown on sapphire contain a high density of threading dislocations, which may accelerate device degradation particularly at high currents. Second, due to the insulating substrate, LEDs on sapphire are normally fabricated in a lateral device configuration. Mismatch between the n-type and p-type current spreading layers may cause severe current crowding and localized self-heating [32–34]. Finally, sapphire has a rather poor thermal conductivity, limiting heat dissipation and, therefore, the maximum operational temperature and power. Homoepitaxial LEDs would overcome all these drawbacks. High material quality, along with the good thermal and electrical conductivity of the substrate, makes homoepitaxial LEDs more suitable for high-current and high-temperature operations.

To examine the impact of device geometry on high-current performance, near-UV LEDs with both lateral and vertical structures were fabricated on HVPE GaN. The chip size was 300 μm × 300 μm. The top contact pattern and schematic cross-section of the LEDs are shown in Fig. 1.27. Some p-type finger projections were

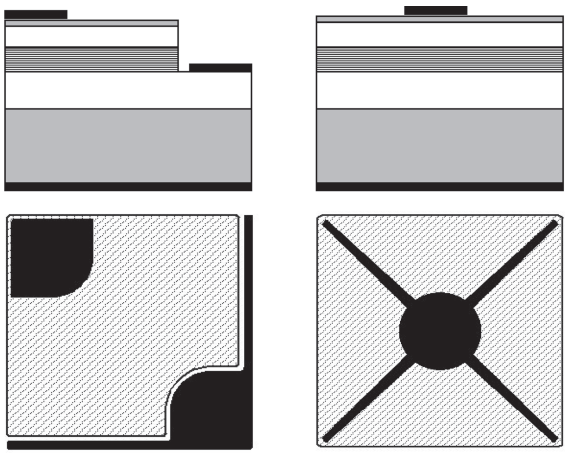

Fig. 1.27 Schematic cross-sections and top contact patterns of lateral and vertical LEDs on sapphire or GaN substrates.

added to the bondpad to alleviate current crowding by reducing the current spreading distance. The vertical LED has an emitting area ~20% larger than the lateral LED because the mesa structure is not needed. The lateral device has a conventional asymmetric structure similar to the LED fabricated on sapphire. Using Eq. (1.1), we calculated the current spreading length L_s in the LED on sapphire to be 250 μm for the measured values of $\rho_p = 2.7\,\Omega\,\text{cm}$, $t_p = 0.2\,\mu\text{m}$, $\rho_n/t_n = 26\,\Omega$, $\rho_t/t_t = 18\,\Omega$, and $r_c = 5 \times 10^{-3}\,\Omega\,\text{cm}^2$. Current crowding takes place at mesa edges and the current density drops to ~1/e under the p-type bondpad. On the contrary, current tends to crowd toward the p-type bondpad in the lateral LED on GaN due to the thick conductive substrate. Uniform current spreading may be achieved by optimizing the transparent contact to meet $\rho_t/t_t = \rho_n/t_n$. However, due to the different temperature dependences of ρ_t and ρ_n, current crowding may occur as the junction temperature increases at high operating currents.

The vertical LED has a symmetric structure and contact geometry similar to conventional AlInGaP LEDs grown on conductive GaAs. Current spreads uniformly under the p-type bondpad metal. The current spreading length is independent of the conductivity of the n-GaN layer and varies approximately as $(\rho_t/t_t)^{1/2}$. By adding the cross-shaped fingers, lateral current paths in the transparent contact are considerably reduced, leading to a nearly uniform current distribution and light emission.

Figure 1.28 compares the forward *I–V* characteristics of the lateral and vertical LEDs. The series resistances of the vertical LED on GaN and the lateral LEDs on GaN and sapphire are 7 Ω, 12.2 Ω, and 14.2 Ω, respectively. The high series resistance of the lateral devices is due largely to an extra voltage drop within the current

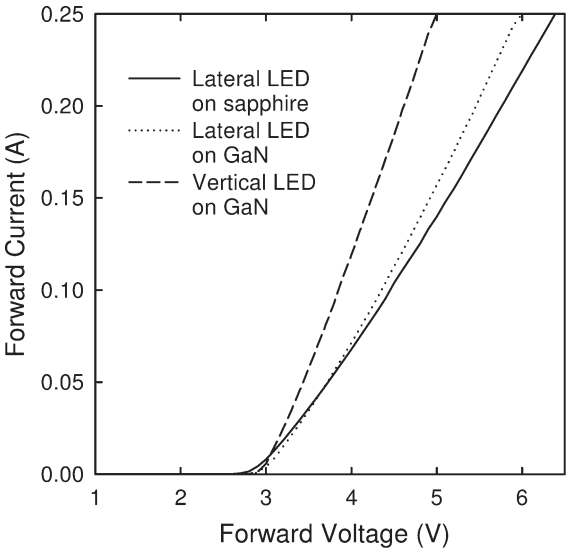

Fig. 1.28 Forward *I–V* characteristics of lateral and vertical LEDs on sapphire or GaN.

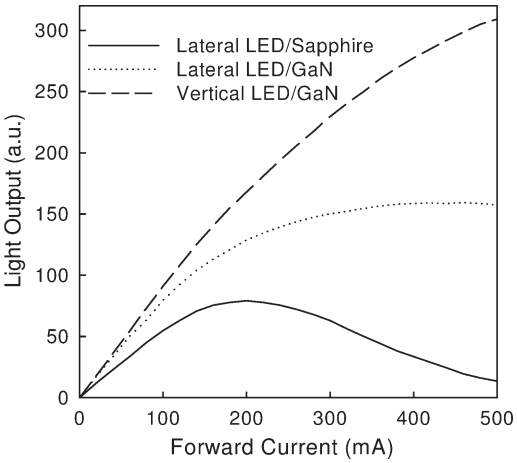

Fig. 1.29 Light output of lateral and vertical LEDs on sapphire or GaN as a function of injection current measured in CW mode.

spreading layers. The forward voltage of the vertical LED at 200 mA is 4.5 V, much lower than 5.8 V for the lateral LED on sapphire. With a much lower series resistance, and therefore a reduced thermal load, the vertical LED has a higher allowable operating temperature and power conversion efficiency.

The output power of the LEDs as a function of injection current measured in CW mode is shown in Fig. 1.29. The homoepitaxial LEDs greatly outperform the LED on sapphire at high injection levels. The output power of the lateral LEDs on sapphire and GaN peaks at ~200 mA and 400 mA, respectively. The power rollover can be attributed to severe current crowding and self-heating effects, which are even more pronounced in the LED on sapphire due to the poor thermal conductivity of sapphire. As the LED junction temperature increases, carrier confinement in the MQWs becomes less efficient, leading to a decreased radiative efficiency. In sharp contrast, the output power of the vertical LED on GaN increases steadily with increasing current and shows no saturation up to 500 mA. At this current, the vertical LED chip has a power conversion efficiency two times higher than the lateral LED on GaN and 28 times higher than the LED on sapphire. These results illustrate the critical need to develop efficient thermal management schemes for high-power LED packages.

LED reliability at high currents was evaluated by stressing the LEDs at 400 mA, which is 20 times higher than standard rated current for most commercially available blue LEDs of a similar size. The average current density in the lateral LEDs was 620 A cm^{-2}, and localized current densities could be much higher due to nonuniform current spreading. Figure 1.30 shows the variation of light output as a function of stress time. The optical power of the vertical LED is essentially unchanged (<1% decrease), suggesting excellent reliability. The lateral LED on

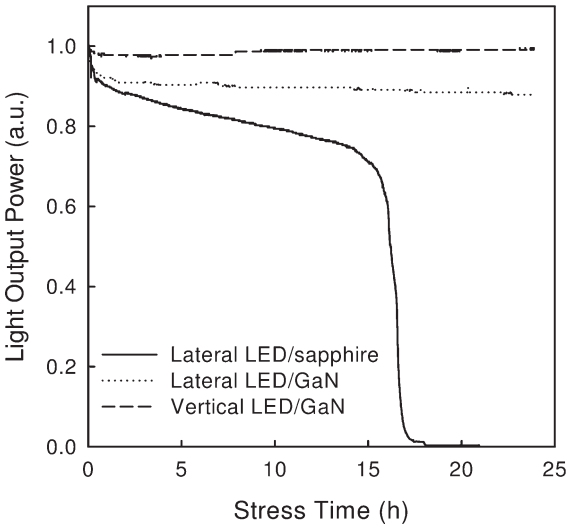

Fig. 1.30 Normalized optical power of lateral and vertical LEDs on sapphire or GaN as a function of stress time. The LEDs were stressed at 400 mA at room temperature.

GaN exhibits a gradual degradation and a 12% decrease after 24 h stress. The light output L is roughly an exponential function of t,

$$L = L_0 \exp(-\beta t) \tag{1.9}$$

and the value of the degradation rate β is determined to be $1.9 \times 10^{-3}\,h^{-1}$. The lateral LED on sapphire also shows a gradual decay during the first 15 h, though with a much higher rate of $1.4 \times 10^{-2}\,h^{-1}$. Further stress leads to a nearly catastrophic failure. The drastic drop in light output is accompanied by the destruction of the p-type contact, suggesting that the device failure may be caused by contact degradation at elevated temperatures.

To glean further insight into the stress failure mechanism, symmetrical lateral LEDs with an n-electrode ring surrounding the mesa were also fabricated on sapphire and stressed under the same conditions. Current spreading was greatly improved in these LEDs and optical degradation was less than 5% after the stress. The slow degradation rate confirms that pre-existing dislocations (~$10^9\,cm^{-2}$) in the LEDs grown on sapphire do not drive the degradation of optical power at current density up to ~700 A cm^{-2}. Threading dislocations in GaN and its alloys have been predicted to have a much lower mobility than those in conventional III–V semiconductors, due partly to a small shear stress for dislocation motion [137].

It is worth mentioning that III–nitride laser diodes (LDs) typically operate at current densities in the kA cm^{-2} range, and therefore are more sensitive to the

presence of the dislocations [138–141]. Indeed, the success of GaN-based LDs is based on the development of the lateral epitaxial overgrowth (LEO) technique [139, 140]. The dislocation density in GaN grown by LEO on sapphire can be reduced to 10^5–$10^7\,cm^{-2}$. The lifetime of LDs grown on LEO GaN was found to be one order of magnitude longer than that of LDs grown on sapphire substrates [139]. The defect density may be further reduced by using LEO in conjunction with the HVPE technique [141]. Homoepitaxy of LD structures on such a low-defect GaN substrate should have a significant positive impact on the device lifetime, particularly at high power consumption.

1.6 LEDs on Other Novel Substrates

Other novel substrates pursued for the epitaxy of III–nitride LEDs can be categorized into two groups: those providing better lattice-constant matching for the nitrides and those producing nonpolar LED structures.

Like bulk GaN, AlN is an ideal substrate for III–nitride epitaxy. It has excellent mechanical strength and thermal stability, and closely matches the crystal structure and lattice parameter of high-Al AlGaN. These properties, along with its UV transparency and high thermal conductivity ($3.2\,W\,cm^{-1}\,K^{-1}$), make it particularly attractive for the growth of deep-UV LEDs. LEDs on AlN substrates must be fabricated in a lateral configuration due to its insulating nature. Native AlN crystals, however, do not exist. To date, sublimation–recondensation has been the most successful technique to produce bulk AlN [142–144]. Recent progress has resulted in production of high-quality AlN crystal exceeding 1 inch in diameter and having a dislocation density less than $10^4\,cm^{-2}$ [143, 144].

Epi-ready AlN substrates with surface roughness ~1 nm can be prepared using chemomechanical polishing [145]. Epitaxial growth on AlN substrates has been found to be limited by the affinity for Al_2O_3 formation at the AlN surface [146]. The dislocation density in AlN and AlGaN epilayers was reported to be $\sim 1 \times 10^8\,cm^{-2}$ [145, 146], much higher than those in the AlN substrates. In situ reflection high-energy electron diffraction revealed crystalline Al_2O_3 islands on the Al face of AlN [146]. The residual oxide islands, which may form by exposure to air, lead to three-dimensional growth and an increased dislocation density in the epilayers. A relatively clean surface can be obtained by exposing AlN to an NH_3 flux to nitridate the surface [146], but a complete removal of the native oxide is needed to obtain high-quality epilayers. Fully strained $Al_{0.5}Ga_{0.5}N$/AlN MQWs have been grown on AlN using MOCVD, which demonstrated photoluminescence at 260 nm with intensity 28 times higher than a similar structure grown on SiC [147]. Nishida et al. [148] reported an AlGaN MQW LED on AlN with a peak wavelength at 345 nm. The output power linearly increased up to 300 mA for a $300\,\mu m \times 300\,\mu m$ flipchip LED, and the maximum optical power was ~1.2 mW. In comparison to similar UV LEDs grown on sapphire, the LED on AlN exhibited a notably higher saturation current, which is attributed to the much higher thermal conductivity of AlN.

Other crystals that may be considered as the substrates of III–nitride LEDs include ZnO, $LiGaO_2$, and ZrB_2. These crystals have a crystalline structure similar to III–nitrides, and their lattice constants are closely matched. These substrates can be selectively etched, facilitating substrate removal for better heat dissipation or light extraction. One major disadvantage of using these substrates is their poor thermal stability under nitride growth conditions [149–152]. For instance, at typical GaN epitaxy temperatures, diffusion and reaction between $LiGaO_2$ and GaN may produce a noncrystalline interfacial layer, degrading the quality of epilayers [150]. InGaN/GaN MQW LEDs have been successfully grown on a ZrB_2 substrate with a low-temperature AlN buffer layer [152]. The buffer layer was deposited at 600 °C, which is lower than the formation temperature of an undesirable ZrBN layer.

All the substrates discussed to this point produce (0001) *c*-plane wurtzite III–nitride materials, as this orientation is favorable for smooth epitaxial growth. In *c*-plane LED structures, there is a strong piezoelectric and spontaneous polarization along the *c*-axis. The built-in electric field separates electron–hole pairs, therefore reducing the radiative recombination efficiency and causing a redshift of the emission peak. A direct strategy to eliminate the polarization effects is to grow LED structures with a nonpolar orientation, such as $(11\bar{2}0)$ *a*-plane and $(10\bar{1}0)$ *m*-plane or with a semipolar orientation such as $(11\bar{2}n)$ and $(10\bar{1}n)$ planes. The use of nonpolar-plane epitaxy allows LED growth in the direction perpendicular to the axis of polarization, whereas semipolar planes allow growth in an off-axis direction from the *c*-plane polarization vector, eliminating or reducing the polarization field in the active region.

Nonpolar LEDs have been grown on *a*-plane HVPE GaN [153], *r*-plane sapphire [152, 154, 155], as well as *m*-plane GaN [156] and 4H-SiC substrates [152, 157]. In most cases, LED performance has been limited by rough morphology, high density of dislocations and stacking faults, which arise from asymmetric off-*c*-axis growth [158]. Recently, the performance of *a*-plane LEDs was significantly improved by using a lateral epitaxially overgrown *a*-plane GaN template [153, 159]. The LEO process yielded *a*-plane GaN with an improved surface morphology and markedly reduced density of dislocations and stacking faults. $In_{0.17}Ga_{0.83}$/GaN MQWs LEDs grown on the template had an output power of 0.24 μW at 20 mA and current-independent emission peak at 413 nm [153]. The latter offers indirect experimental evidence that the polarization field is negligible in these LEDs. Blue LEDs grown on *m*-plane GaN showed a similar optical efficiency, but a significant current-induced blueshift in peak emission, which was attributed to band filling of localized states [156].

Polarized light emission from *a*-plane and *m*-plane LEDs has been predicted by valence band calculations of wurtzite GaN assuming a strong *c*-axis polarization [160–162]. In MQW LEDs, the interaction of the multiple valence bands with the strong *c*-axis polarization dipole supports radiative recombination at specific optical polarizations depending on the orientation of the light-emitting QWs with respect to the *c*-axis. Polarized light emission along the $\langle 1\bar{1}00\rangle$ direction has been observed from an *m*-plane blue LED [157, 162]. The emitted light was partially polarized in the $\langle 11\bar{2}0\rangle$ direction with a polarization ratio of 0.17 [162]. Preferential

optical polarization can be useful for liquid-crystal display applications and other applications where polarized light is essential for operation.

1.7 Conclusions

Since the development of high-quality GaN and AlN buffer layers, sapphire and SiC have become the dominant substrates for III–nitride LEDs. High-brightness InGaN-based green, blue and near-UV LEDs have been demonstrated and commercialized despite the presence of a high dislocation density in the heteroepitaxial structures. Localization effects induced by In compositional fluctuation are believed to be responsible for the enhanced radiative process. The well-established growth and processing technologies for LEDs on sapphire and SiC justify the enormous ongoing efforts to develop high-efficiency and low-cost LEDs on these substrates for next-generation lighting. Making solid-state lighting a reality will require further improvements in LED efficiency and reliability, and reductions in cost. Optimizing reactor design and growth recipes, and developing novel light extraction approaches are expected to provide opportunities for breakthrough.

The low cost and high quality of Si, and the possibility of integration with Si electronics, make it an attractive substrate for III–nitride LED growth. Blue LEDs with reasonable performance have been made on up to 6 inch Si substrates despite a large mismatch between Si and GaN. It is likely that the use of Si substrates will be limited to low-cost and low-brightness light-emitting devices, unless the epitaxy quality is considerably improved and an economical film-transfer process is developed.

Sapphire will likely be the substrate of choice for deep-UV LEDs due in part to its transparency. Milliwatt UV LEDs with emission wavelengths as short as 250 nm have emerged in the past several years. Further improvement in LED performance is expected in the near future as the heteroepitaxy of AlGaN materials on sapphire is refined. AlN is a much closer lattice and thermal match for High-Al content AlGaN heterostructures. If bulk AlN or AlGaN becomes commercially available, these materials would be the best choice as the substrate for deep UV LEDs.

Free-standing GaN is a nearly perfect chemical, crystallographic, lattice-constant, and thermal-expansion match to LED heterostructures. Homoepitaxy would improve the quality and yield of LED production, and simplify the procedures for growth, fabrication, packaging, and thermal designs. Homoepitaxial LEDs have proven to be suitable for high-power and highly reliable operation, and thus more light can be delivered from a single package. Unfortunately the growth of bulk GaN is still in its infancy. Bulk GaN grown by HVPE has relatively poor crystalline quality, whereas crystals produced using solution growth techniques have slow rate and small size limitations. The lack of low-cost, large-size, and flawless GaN wafers remains an obstacle. This obstacle must be overcome before III–nitride LEDs grown on GaN substrates have an impact on the development of high-brightness and cost-efficient solid-state lighting sources.

Acknowledgments

The author would like to thank his collaborators S. F. LeBoeuf, J. Teetsov, J. W. Kretchmer, S. D. Arthur, D. W. Merfeld, and M. P. D'Evelyn at GE Global Research Center, and C. H. Yan and W. Wang at Lumei Optoelectronics.

References

1 S. Nakamura, S. J. Pearton, and G. Fasol, *The Blue Laser Diode*, Springer-Verlag, Heidelberg, Germany, **2000**.
2 M. A. Khan, M. Shatalov, H. P. Maruska, H. M. Wang, and E. Kuokstis, *Jpn. J. Appl. Phys.* **2005**, 44, 7191.
3 J. Y. Tsao, *IEEE Circuits and Devices* **2004**, 5/6, 28.
4 S. F. Chichibu, Y. Kawakami, and T. Sota, in *Introduction to Nitride Semiconductor Blue Lasers and Light Emitting Diodes*, ed. S. Nakamura and S. F. Chichibu, Taylor and Francis, New York, **2000**.
5 X. Xu, R. P. Vaudo, C. Lario, A. Saland, G. R. Brandes, and J. Chaudhuri, *J. Cryst. Growth* **2002**, 246, 223.
6 J. C. Rojo, G. A. Slack, K. Morgan, B. Raghothamachar, M. Dudley, and L. J. Schowalter, *J. Cryst. Growth* **2001**, 231, 317.
7 S. P. DenBaars and S. Keller, in *Gallium Nitride (II)*, ed. J. I. Pankove and T. D. Moustakas, Academic Press, San Diego, **1998**.
8 H. Amano, I. Akasaki, T. Kozawa, K. Hiramatsu, N. Sawak, K. Ikeda, and Y. Ishi, *J. Lumin.* **1988**, 40–41, 121.
9 S. Nakamura, N. Iwasa, M. Senoh, and T. Mukai, *Jpn. J. Appl. Phys.* **1992**, 31, 1258.
10 H. Amano, N. Sawaki, I. Akasaki, and Y. Toyoda, *Appl. Phys. Lett.* **1986**, 48, 353.
11 S. Nakamura, *Jpn. J. Appl. Phys.* **1991**, 30, L1705.
12 H. Kawakami, K. Sakurai, K. Tsubouchi, and N. Mikoshiba, *Jpn. J. Appl. Phys.* **1998**, 27, L161.
13 T. D. Moustakas, T. Lei, and R. J. Molnar, *Physica B* **1993**, 185, 36.
14 S. Nakamura, T. Mukai, and M. Senoh, *Appl. Phys. Lett.* **1994**, 64, 1687.
15 S. Nakamura, M. Senoh, N. Iwasa, S. Nagahama, T. Yamada, T. Mukai, *Jpn. J. Appl. Phys.* **1995**, 34, L1332.
16 D. Steigerwald, S. Rudaz, H. Liu, R. S. Kern, W. Götz, and R. Fletcher, *JOM* **1997**, 49, 18.
17 M. Koike, N. Shibata, H. Kato, and Y. Takahashi, *IEEE J. Sel. Top. Quantum Electron*, **2002**, 8, 271.
18 J. P. Zhang, A. Chitnis, V. Adivarahan, S. Wu, V. Mandavilli, R. Pachipulusu, M. Shatalov, G. Simin, J. W. Yang, and M. Asif Khan, *Appl. Phys. Lett.* **2002**, 81, 4910.
19 A. A. Allerman, M. H. Crawford, A. J. Fischer, K. H. A. Bogart, S. R. Lee, D. M. Follstaedt, P. P. Provencio, and D. D. Koleske, *J. Cryst. Growth*, **2004**, 272, 227.
20 M. Leszczynski, T. Suski, H. Teisseyre, P. Perlin, I. Grzegory, J. Jun, S. Porowski, and T. D. Moustakas, *J. Appl. Phys.* **1994**, 76, 4909.
21 L. T. Romano, C. G. Van de Walle, J. W. Ager III, W. Götz, and R. S. Kern, *J. Appl. Phys.* **2000**, 87, 7745.
22 J. Zhang, E. Kuokstis, Q. Fareed, H. Wang, J. Yang, G. Simin, M. Asif Khan, R. Gaska, and M. Shur, *Appl. Phys. Lett.* **2001**, 79, 925.
23 S. D. Lester, F. A. Ponce, M. G. Craford, and D. A. Steigerwald, *Appl. Phys. Lett.* **1995**, 66, 1249.
24 D. Kapolnek, X. H. Wu, B. Heying, S. Keller, U. K. Mishra, S. P. DenBaars, and S. J. Speck, *Appl. Phys. Lett.* **1995**, 67, 1541.
25 X. H. Wu, C. R. Elsass, A. Abare, M. Mack, S. Keller, P. M. Petroff, S. P. DenBaars, J. S. Speck, and S. J. Rosner, *Appl. Phys. Lett.* **1998**, 72, 692.
26 D. I. Florescu, S. M. Ting, J. C. Ramer, D. S. Lee, V. N. Merai, A. Parkeh, D. Lu,

E. A. Armour, and L. Chernyak, *Appl. Phys. Lett.* **2003**, 83, 33.
27 Z. Liliental-Weber, Y. Chen, S. Ruvimov, and J. Washburn, *Phys. Rev. Lett.* **1997**, 79, 2835.
28 A. H. Herzog, D. L. Keune, and M. G. Craford, *J. Appl. Phys.* **1972**, 43, 600.
29 S. D. Lester, F. A. Ponce, M. G. Craford, and D. A. Steigerwald, *Appl. Phys. Lett.* **1996**, 66, 1249.
30 T. Mukai and S. Nakamura, *Jpn. J. Appl. Phys.* **1999**, 38, 5735.
31 S. Chichibu, T. Aznhata, T. Sota, and S. Nakamura, *Appl. Phys. Lett.* **1996**, 69, 4188.
32 X. A. Cao, E. B. Stokes, P. Sandvik, N. Taskar, J. Kretchmer, and D. Walker, *Solid State Electron.* **2002**, 46, 1235.
33 H. Kim, S. J. Park, H. Hwang, and N. M. Park, *Appl. Phys. Lett.* **2002**, 81, 1326.
34 X. Guo, Y. L. Li, and E. F. Schubert, *Appl. Phys. Lett.* **2001**, 79, 1936.
35 J. K. Ho, C. S. Jong, C. C. Chiu, C. N. Huang, C. Y. Chen, and K. Shih, *Appl. Phys. Lett.* **1999**, 74, 1275.
36 J. K. Ho, C. S. Jong, C. C. Chiu, C. N. Huang, K., K. Shih, L. C. Chen, F. R. Chen, and J. J. Kai, *J. Appl. Phys.* **1999**, 86, 4491.
37 J. O. Song, J. S. Kwak, Y. Park, and T. Y. Seong, *Appl. Phys. Lett.* **2004**, 85, 6374.
38 J. O. Song, J. S. Kwak, Y. Park, and T. Y. Seong, *Appl. Phys. Lett.* **2005**, 86, 213505.
39 S. P. Jung, D. Ullery, C. H. Lin, H. P. Lee, J. H. Lim, D. K. Hwang, J. Y. Kim, E. J. Yang, and S. J. Park, *Appl. Phys. Lett.* **2005**, 87, 181107.
40 X. Guo and E. F. Schubert, *Appl. Phys. Lett.* **2001**, 78, 3337.
41 A. Chitnis, J. Sun, V. Mandavilli, R. Pachipulusu, S. Wu, M. Gaevski, V. Adivarahan, J. P. Zhang, M. A. Khan, A. Sarua, and M. Kuball, *Appl. Phys. Lett.* **2002**, 81, 3491.
42 S. M. Sze, *Physics of Semiconductor Devices*, 2nd edition, Wiley, New York, **1981**.
43 G. Franssen, E. Staszewska, R. Piotrzkowski, T. Suski, and P. Perlin, *J. Appl. Phys.* **2003**, 94, 6122.
44 D. J. Dumin and G. L. Pearson, *J. Appl. Phys.* **1965**, 36, 3418.
45 X. A. Cao, E. B. Stokes, P. Sandvik, S. F. LeBoeuf, J. Kretchmer, and D. Walker, *IEEE Electron Dev. Lett.* **2002**, 23, 535.
46 A. R. Riben and D. L. Feucht, *Solid-State Electron.* **1966**, 9, 1055.
47 S. R. Forrest, M. Didomernico, Jr., R. G. Smith, and H. J. Stocker, *Appl. Phys. Lett.* **1980**, 36, 580.
48 J. B. Fedison, T. P. Chow, H. Lu, and I. B. Bhat, *Appl. Phys. Lett.* **1998**, 72, 2841.
49 P. G. Eliseev, P. Perlin, J. Furioli, J. Mu, M. Banas, P. Sartori, J. Mu, and M. Osinski, *J. Electron. Mater.* **1997**, 26, 311.
50 Y. Narukawa, Y. Kawakami, S. Fujita, S. Fujita, and S. Nakamura, *Phys. Rev. B* **1997**, 55, 1938.
51 R. W. Martin, P. G. Middleton, K. P. O'Donnell, and W. Van der Stricht, *Appl. Phys. Lett.* **1999**, 74, 263.
52 H. C. Yang, P. F. Kuo, T. Y. Lin, Y. F. Chen, K. H. Chen, L. C. Chen, and J. I. Chyi, *Appl. Phys. Lett.* **2000**, 76, 3712.
53 L. Nistor, H. Bender, A. Vantomme, M. F. Wu, J. V. Lauduyt, K. P. O'Donnell, R. Martin, K. Jacobs, and I. Moerman, *Appl. Phys. Lett.* **2000**, 77, 507.
54 S. Chichibu, K. Wada, and S. Nakamura, *Appl. Phys. Lett.* **1997**, 71, 2346.
55 K. P. O'Donnell, R. W. Martin, and P. G. Middleton, *Phys. Rev. Lett.* **1999**, 82, 237.
56 C. H. Chen, L. Y. Huang, Y. F. Chen, H. X. Jiang, and J. Y. Lin, *Appl. Phys. Lett.* **2002**, 80, 1397.
57 G. Tamulaitis, K. Kazlauskas, S. Jursenas, A. Zukauskas, M. A. Khan, J. W. Yang, J. Zhang, G. Simin, M. S. Shur, and R. Gaska, *Appl. Phys. Lett.* **2000**, 77, 2136.
58 M. A. Khan, V. Adivarahan, J. P. Zhang, C. Chen, E. Kuokstis, A. Chitnis, M. Shatalov, J. W. Yang, and G. Simin, *Jpn. J. Appl. Phys.* **2001**, 40, L1308.
59 H. Hirayama, *J. Appl. Phys.* **2005**, 97, 091101.
60 F. G. McIntosh, K. S. Boutros, J. C. Roberts, S. M. Bedair, E. L. Piner, and N. A. El-Masry, *Appl. Phys. Lett.* **1996**, 68, 40.
61 F. Bernardini, V. Fiorentini, F. Della Sala, A. Di Carlo, and P. Lugli, *Phys. Rev. B* **1999**, 60, 8849.

62 T. Deguchi, A. Shikanai, K. Torii, T. Sota, S. Chichibu, and S. Nakamura, *Appl. Phys. Lett.* **1998**, 72, 3329.

63 T. Takeuchi, S. Sota, M. Katsuragawa, M. Komori, H. Takeuchi, H. Amano, and I. Akasaki, *Jpn. J. Appl. Phys.* **1997**, 36, L382.

64 Y. D. Qi, H. Liang, D. Wang, Z. D. Lu, W. Tang, and K. M. Lau, *Appl. Phys. Lett.* **2005**, 86, 101903.

65 Y. H. Cho, J. J. Song, S. Keller, M. S. Minsky, E. Hu, U. K. Mishra, and S. P. DenBaars, *Appl. Phys. Lett.* **1998**, 73, 1128.

66 A. E. Yunovich and S. S. Mamakin, *Mat. Res. Soc. Symp. Proc.* **2002**, 722, K2.4.1.

67 Y. H. Cho, G. H. Gainer, A. J. Fischer, J. J. Song, S. Keller, U. K. Mishra, and S. P. DenBaars, *Appl. Phys. Lett.* **1998**, 73, 1370.

68 W. Shan, T. J. Schmidt, X. H. Yang, S. J. Hwang, J. J. Song, and B. Goldenberg, *Appl. Phys. Lett.* **1995**, 66, 985.

69 I. L. Krestnikov, N. N. Ledentsov, A. Hoffmann, D. Bimberg, A. V. Sakharov, W. V. Lundin, A. F. Tsatsulnikov, A. S. Usikov, Z. I. Alferov, Y. G. Musikhin, and D. Gerthsen, *Phys. Rev. B* **2002**, 66, 155310.

70 M. Smith, G. D. Chen, J. Y. Lin, H. X. Jiang, M. Asif Khan, and Q. Chen, *Appl. Phys. Lett.* **1996**, 69, 2837.

71 B. Monemar, *Phys. Rev. B* **1974**, 10, 676.

72 S. Nakamura, *JSAP International*, **2000**, 1, 5.

73 M. Khizar, Z. Y. Fan, K. H. Kim, J. Y. Lin, and H. X. Jiang, *Appl. Phys. Lett.* **2005**, 85, 173504.

74 K. Mayes, A. Yasan, R. McClintock, D. Shiell, S. R. Darvish, P. Kung, and M. Razeghi, *Appl. Phys. Lett.* **2004**, 84, 1046.

75 A. J. Fischer, A. A. Allerman, M. H. Crawford, K. H. A. Bogart, S. R. Lee, R. J. Kaplar, W. W. Chow, S. R. Kurtz, K. W. Fullmer, and J. J. Figiel, *Appl. Phys. Lett.* **2004**, 84, 3394.

76 J. P. Zhang, S. Wu, S. Rai, V. Mandavilli, V. Adivarahan, A. Chitnis, M. Shatalov, and M. A. Khan, *Appl. Phys. Lett.* **2003**, 83, 3456.

77 A. R. Riben and D. L. Feucht, *Solid-State Electron.* **1966**, 9, 1055.

78 X. A. Cao, S. F. Leboeuf, L. R. Rowland, and H. Liu, *J. Electron. Mater.* **2003**, 32, 316.

79 J. J. Wierer, D. A. Steigerwald, M. R. Krames, J. J. O'Shea, M. J. Ludowise, G. Christenson, Y.-C. Shen, C. Lowery, P. S. Martin, S. Subramanya, W. Gotz, N. F. Gardner, R. S. Kern, and S. A. Stockman, *Appl. Phys. Lett.* **2001**, 78, 3379.

80 J. C. Bhat, A. Kim, D. Collins, R. Fletcher, R. Khare, and S. Rudaz, *ISCS*, Tokyo, Japan, October **2001**.

81 T. Fujii, Y. Gao, R. Sharma, E. L. Hu, S. P. DenBaars, and S. Nakamura, *Appl. Phys. Lett.* **2004**, 84, 855.

82 C. Huh, K. S. Lee, E. J. Kang, and S. J. Park, *J. Appl. Phys.* **2003**, 93, 9383.

83 K. Tadatomo, H. Okagawa, Y. Ohuchi, T. Tsunekawa, Y. Imada, M. Kato, and T. Taguchi, *Jpn. J. Appl. Phys.* **2001**, 40, L583.

84 M. Yamada, T. Mitani, Y. Narukawa, S. Shioji, I. Niki, S. Sonobe, K. Deguchi, M. Sano, and T. Mukai, *Jpn. J. Appl. Phys.* **2002**, 41, L1431.

85 M. Khizar, Z. Y. Fan, K. H. Kim, J. Y. Lin, and H. X. Jiang, *Appl. Phys. Lett.* **2005**, 86, 173504.

86 T. N. Oder, K. H. Kim, J. Y. Lin, and H. X. Jiang, *Appl. Phys. Lett.* **2004**, 84, 466.

87 J. J. Wierer, M. R. Krames, J. E. Epler, N. F. Gardner, M. G. Craford, J. R. Wendi, J. A. Simmons, and M. M. Sigalas, *Appl. Phys. Lett.* **2004**, 84, 3885.

88 K. Okamoto, I. Niki, A. Shvartser, Y. Narukawa, T. Mukai, and A. Scherer, *Nat. Mater.* **2004**, 3, 601.

89 J. Edmond and J. Lagaly, *JOM* **1997**, 9, 24.

90 V. Harle, B. Hahn, H. J. Lugaauer, G. Bruderl, D. Eisert, U. Strauss, A. Lell, and N. Hiller, *Compound Semiconductors* **2000**, 6, 81.

91 F. A. Ponce, B. S. Krusor, J. S. Major, Jr., W. E. Plano, and D. F. Welch, *Appl. Phys. Lett.* **1995**, 67, 410.

92 T. W. Weeks, Jr., M. D. Bremser, K. S. Ailey, E. Carlson, W. G. Perry, and R. F. Davis, *Appl. Phys. Lett.* **1995**, 67, 401.

93 S. Tanaka, S. Iwai, and Y. Aoyagi, *J. Cryst. Growth* **1997**, 170, 329.

94 P. Waltereit, O. Brandt, A. Trampert, M. Ramsteiner, M. Reiche, M. Qi, and K. H. Ploog, *Appl. Phys. Lett.* **1999**, 74, 3660.

95 M. R. Krames, M. Ochiai-Holcomb, G. E. Hofler, C. Carter-Coman, E. I. Chen, I. H. Tan, P. Grillot, N. F. Gardner, H. C. Chui, J.-W. Huang, S. A. Stockman, F. A. Kish, and M. G. Craford, *Appl. Phys. Lett.* **1999**, 75, 2365.

96 J. Edmond, D. Emerson, M. Bergmann, K. Haberer, and C. Hussell, *ICSCRM*, Pittsburgh, PA, **2005**.

97 S. Guha and N. A. Bojarczuk, *Appl. Phys. Lett.* **1998**, 73, 1487.

98 G. Kipshidze, V. Kuryatkov, B. Borisov, M. Holtz, S. Nikishin, and H. Temkin, *Appl. Phys. Lett.* **2002**, 80, 3682.

99 C. A. Tran, A. Osinski, R. F. Karlicek, Jr., and I. Berishev, *Appl. Phys. Lett.* **1999**, 75, 1494.

100 A. Dadgar, M. Poschenrieder, J. Bläsing, K. Fehse, A. Diez, and A. Krost, *Appl. Phys. Lett.* **2002**, 80, 3670.

101 H. Ishikawa, B. Zhang, K. Asano, T. Egawa, and T. Jimbo, *J. Cryst. Growth* **2004**, 272, 322.

102 B. Zhang, T. Egawa, H. Ishikawa, Y. Liu, and T. Jimbo, *Appl. Phys. Lett.* **2005**, 86, 071113.

103 J. Li, J. Y. Lin, and H. X. Jiang, MRS Fall Meeting, Boston, MA, **2004**.

104 H. P. D. Schenk, G. D. Kipshidze, V. B. Lebedev, S. Shokhovets, R. Goldhahn, J. Kräußlich, A. Fissel, and W. Richter, *J. Cryst. Growth* **1999**, 201–202, 359.

105 S. A. Nikishin, N. N. Faleev, A. S. Zubrilov, V. G. Antipov, and H. Temkin, *Appl. Phys. Lett.* **2000**, 76, 3028.

106 H. Marchand, L. Zhao, N. Zhang, B. Moran, R. Coffie, U. K. Mishra, J. S. Speck, S. P. DenBaars, and J. A. Freitas, *J. Appl. Phys.* **2001**, 89, 7846.

107 M.-H. Kim, Y.-C. Bang, N.-M. Park, C.-J. Choi, T.-Y. Seong, and S.-J. Park, *Appl. Phys. Lett.* **2001**, 78, 2858.

108 E. Feltin, B. Beaumont, M. Laügt, P. de Mierry, P. Vennéguès, H. Lahrèche, M. Leroux, and P. Gibart, *Appl. Phys. Lett.* **2001**, 79, 3230.

109 W. S. Wong, T. Sands, N. W. Cheung, M. Kneissl, D. P. Bour, P. Mei, L. T. Romano, and N. M. Johnson, *Appl. Phys. Lett.* **2000**, 77, 2822.

110 B. S. Tan, S. Yuan, and X. J. K. Kang, *Appl. Phys. Lett.* **2004**, 84, 2757.

111 S. Porowski and I. Grzegory, in *GaN and Related Materials*, ed. S. J. Pearton, Gordon and Breach, New York, p. 295, **1997**.

112 S. Porowski, *J. Cryst. Growth* **1996**, 166, 583.

113 S. Sakai, S. Sato, T. Sugahara, Y. Naoi, S. Kurai, K. Yamashita, S. Tottori, M. Hao, K. Wada, and K. Nishino, *Mater. Sci. Forum* **1998**, 264/268, 1107.

114 T. Inoue, Y. Seki, O. Oda, S. Kurai, Y. Yamada, and T. Taguchi, *Phys. Stat. Sol. (b)* **2001**, 223, 15.

115 C. M. Balkas, Z. Sitar, L. Bergman, I. K. Shmagin, J. F. Muth, R. Kolbas, R. J. Nemanich, and R. F. Davis, *J. Cryst. Growth* **2000**, 208, 100.

116 Y. Kumagai, H. Murakami, A. Koukitu, K. Takemoto, and H. Seki, *Jpn. J. Appl. Phys.* **2000**, 39, L703.

117 K. Lee and K. Auh, *MRS Internet J. Nitride Semicond. Res.* **2001**, 6, 4.

118 D. Gogova, A. Kasic, H. Larsson, C. Hemmingsson, B. Monemar, F. Tuomisto, K. Saarinen, L. Dobos, B. Pecz, P. Gibart, and B. Beaumont, *J. Appl. Phys.* **2004**, 96, 799.

119 X. Xu, R. P. Vaudo, C. Loria, A. Salant, G. R. Brandes, and J. Chaudhuri, *J. Cryst. Growth* **2002**, 246, 223.

120 X. Xu, R. P. Vaudo, and G. R. Brandes, *Opt. Mater.* **2003**, 23, 1.

121 X. Xu, R. P. Vaudo, J. Flynn, J. Dion, and G. R. Brandes, *Phys. Stat. Sol. (a)* **2005**, 202, 727.

122 C. R. Miskys, M. K. Kelly, O. Ambacher, G. Martinez-Criado, and M. Stutzmann, *Appl. Phys. Lett.* **2000**, 77, 1858.

123 M. Schauler, F. Eberhard, C. Kirchner, V. Schwegler, A. Pelzmann, M. Kamp, K. J. Ebeling, F. Bertram, T. Riemann, J. Christen, P. Prystawko, M. Leszczynski, I. Grzegory, and S. Porowski, *Appl. Phys. Lett.* **1999**, 74, 1123.

124 X. A. Cao, H. Lu, S. F. LeBoeuf, C. Cowen, S. D. Arthur, and W. Wang, *Appl. Phys. Lett.* **2005**, 87, 053503.

125 I. Arslan and N. D. Browning, *Phys. Rev. Lett.* **2003**, 91, 165501–1.

126 A. Pelzmann, C. Kirchner, M. Mayer, V. Schwegler, M. Schauler, M. Kamp, K. J. Ebeling, I. Grzegory, M. Leszczynski, G. Nowak, and S. Porowski, *J. Cryst. Growth* **1998**, 189–190, 167.

127 G. Franssen, E. Litwin-Staszewska, R. Piotrzkowski, T. Suski, and P. Perlin, *J. Appl. Phys.* **2003**, 94, 6122.

128 X. A. Cao, J. Teetsov, F. Shahedipour-Sandvik, and S. D. Arthur, *J. Cryst. Growth* **2004**, 264, 172.

129 Y. Chen, T. Takeuchi, H. Amano, I. Akasaki, N. Yamada, Y. Kaneko, and S. Y. Wang, *Appl. Phys. Lett.* **1998**, 72, 710.

130 E. J. Miller, D. M. Schaadt, E. T. Yu, C. Poblenz, C. Elsass, and J. S. Speck, *J. Appl. Phys.* **2002**, 91, 9821.

131 J. W. P. Hsu, M. J. Manfra, D. V. Lang, S. Richter, S. N. G. Chu, A. M. Sergent, R. N. Kleiman, L. N. Pfeiffer, and R. J. Molnar, *Appl. Phys. Lett.* **2001**, 78, 1685.

132 A. A. Pomarico, D. Huang, J. Dickinson, A. A. Baski, R. Cingolani, H. Morkoc, and R. Molnar, *Appl. Phys. Lett.* **2003**, 82, 1890.

133 T. Nishida, H. Saito, and N. Kobayashi, *Appl. Phys. Lett.* **2001**, 79, 711.

134 A. Yasan, R. McClintock, K. Mayes, S. R. Darvish, H. Zhang, P. Kung, M. Razeghi, S. K. Lee, and J. Y. Han, *Appl. Phys. Lett.* **2002**, 81, 2151.

135 G. A. Garrett, C. J. Collins, A. V. Sampath, H. Shen, M. Wraback, S. F. LeBoeuf, J. Flynn, and G. Brandes, *Phys. Stat. Sol. (c)* **2005**, 2, 2332.

136 M. G. Craford, *Proc. SPIE* **2002**, 4776, 1.

137 L. Sugiura, *Appl. Phys. Lett.* **1997**, 70, 1317.

138 M. Kneissl, D. P. Bour, L. Romano, C. G. Van de Walle, J. E. Northrup, W. S. Wong, D. W. Treat, M. Teepe, T. Schmidt, and N. M. Johnson, *Appl. Phys. Lett.* **2000**, 77, 1931.

139 S. Nakamura, M. Senoh, S. Nagahama, N. Iwasa, T. Yamada, T. Matsushita, H. Kiyoku, and Y. Sugimoto, *Appl. Phys. Lett.* **1998**, 72, 211.

140 S. Nakamura, M. Senoh, S. Nagahama, N. Iwasa, T. Matsushita, and T. Mukai, *Appl. Phys. Lett.* **2000**, 76, 22.

141 S. Nakamura, M. Senoh, S. Nagahama, N. Iwasa, T. Yamada, T. Matsushita, H. Kiyoku, Y. Sugimoto, T. Kozaki, H. Umemoto, M. Sano, and K. Chocho, *Appl. Phys. Lett.* **1998**, 73, 832.

142 G. A. Slack and T. F. McNelly, *J. Cryst. Growth* **1976**, 34, 163.

143 J. C. Rojo, G. A. Slack, K. Morgan, B. Raghothamachar, M. Dudley, and L. J. Schowalter, *J. Cryst. Growth* **2001**, 231, 317.

144 L. J. Schowalter, G. A. Slack, J. B. Whitlock, K. Morgan, S. B. Schujman, B. Raghothamachar, M. Dudley, and K. R. Evans, *Phys. Stat. Sol. (c)* **2003**, 0, 1997.

145 J. C. Rojo, L. J. Schowalter, R. Gaska, M. S. Shur, M. A. Khan, J. Yang, and D. D. Koleske, *J. Cryst. Growth* **2002**, 240, 508.

146 S. A. Nikishin, B. A. Borisov, A. Chandolu, V. V. Kuryatkov, H. Temkin, M. Holtz, E. N. Mokhov, Y. Makarov, and H. Helava, *Appl. Phys. Lett.* **2004**, 85, 4355.

147 R. Gaska, C. Chen, J. Yang, E. Kuokstis, A. Khan, G. Tamulaitis, I. Yilmaz, M. S. Shur, J. C. Rojo, and L. J. Schowalter, *Appl. Phys. Lett.* **2002**, 81, 4658.

148 T. Nishida, T. Makimoto, H. Saito, and T. Ban, *Appl. Phys. Lett.* **2004**, 84, 1002.

149 G. Namkoong, S. Burnham, K. K. Lee, E. Trybus, W. A. Doolittle, M. Losurdo, P. Capezzuto, G. Bruno, B. Nemeth, and J. Nause, *Appl. Phys. Lett.* **2005**, 87, 184104.

150 W. A. Doolittle and A. S. Brown, *Solid State Electron.* **2000**, 44, 229.

151 S. Kang, W. A. Doolittle, A. S. Brown, and S. R. Stock, *Appl. Phys. Lett.* **1999**, 74, 3380.

152 S. Kamiyama, M. Iwaya, H. Amano, and I. Akasaki, *Mater. Res. Soc. Symp. Proc.* **2005**, 831,

153 A. Chakraborty, B. A. Haskell, S. Keller, J. S. Speck, S. P. DenBaars, S. Nakamura, and U. K. Mishra, *Appl. Phys. Lett.* **2004**, 85, 5143.

154 A. Chitnis, C. Chen, V. Adivarahan, M. Shatalov, E. Kuokstis, V. Mandavilli, J. Yang, and M. A. Khan, *Appl. Phys. Lett.* **2004**, 84, 3663.

155 C. Chen, V. Adivarahan, J. Yang, M. Shatalov, E. Kuokstis, and M. A. Khan, *Jpn. J. Appl. Phys.* **2003**, 42, L1039.

156 A. Chakraborty, B. A. Haskell, S. Keller, J. S. Speck, S. P. Denbaars, S. Nakamura, and U. K. Mishra, *Jpn. J. Appl. Phys.* **2005**, 44, L173.

157 N. F. Gardner, J. C. Kim, J. J. Wierer, Y. C. Shen, and M. R. Krames, *Appl. Phys. Lett.* **2005**, 86, 111101.

158 M. D. Craven, S. H. Lim, F. Wu, J. S. Speck, and S. P. DenBaars, *Appl. Phys. Lett.* **2002**, 81, 469.

159 W. H. Sun, J. W. Yang, C. Q. Chen, J. P. Zhang, M. E. Gaevski, E. Kuokstis, V. Adivarahan, H. M. Wang, Z. Gong, M. Su, and M. A. Khan, *Appl. Phys. Lett.* **2003**, 83, 2599.

160 K. Domen, K. Horino, A. Kuramata, and T. Tanahashi, *Appl. Phys. Lett.* **1997**, 71, 1996.

161 A. Niwa, T. Ohtoshi, and T. Kuroda, *Jpn. J. Appl. Phys.* **1996**, 35, L599.

162 H. Masui, A. Chakraborty, B. A. Haskell, U. K. Mishra, J. S. Speck, S. Nakamura, and S. P. DenBaars, *Jpn. J. Appl. Phys.* **2005**, 44, L1329.